TOPICAL REVIEW

Carbon-based nanotechnology on a supercomputer

David Tománek

Physics and Astronomy Department, Michigan State University, East Lansing, MI 48824-2320, USA

Abstract
The quantum nature of phenomena dominating the behaviour of nanostructures raises new challenges when trying to predict and understand the physical behaviour of these systems. Addressing this challenge is imperative in view of the continuous reduction of device sizes, which is rapidly approaching the atomic level. Since even the most advanced experimental observations are subject to being fundamentally influenced by the measurement itself, new approaches must be sought to design and test future building blocks of nanotechnology. In this respect, high-performance computing, allowing predictive large-scale computer simulations, has emerged as an indispensable tool to foresee and interpret the physical behaviour of nanostructures, thus guiding and complementing the experiment. This contribution will review some of the more intriguing phenomena associated with nanostructured carbon, including fullerenes, nanotubes and diamondoids. Due to the stability of the sp^2 bond, carbon fullerenes and nanotubes are thermally and mechanically extremely stable and chemically inert. They contract rather than expand at high temperatures, and are unparalleled thermal conductors. Nanotubes may turn into ballistic electron conductors or semiconductors, and even acquire a permanent magnetic moment. In nanostructures that form during a hierarchical self-assembly process, even defects may play a different, often helpful role. sp^2 bonded nanostructures may change their shape globally by a sequence of bond rotations, which turn out to be intriguing multi-step processes. At elevated temperatures, and following photo-excitations, efficient self-healing processes may repair defects, thus answering an important concern in molecular electronics.

(Some figures in this article are in colour only in the electronic version)

Contents

1. Introduction

In his inspiring contribution entitled 'There is Plenty of Room at the Bottom' [1], Richard Feynman pointed out the untapped potential of functional nanostructures, assembled with atomic precision, to influence our every-day lives. Presented in 1959, thus pre-dating the era of integrated circuits displaying an ever-increasing component density, this revolutionary talk may well be considered the founding moment of the emerging interdisciplinary field called 'nanotechnology'.

Interest in carbon nanostructures has been growing steadily since the synthesis of carbon fibres and transmission electron microscopy observations of their core structure [2]. The decisive boost for the field of nanocarbons, however, came with the observation of the C_{60} 'buckyball' molecule [3] and carbon nanotubes [4]. These atomically well-defined systems form spontaneously from a variety of carbon-containing compounds by catalytic or autocatalytic processes, often involving very high temperatures. Exhibiting an unusual combination of mechanical, thermal, electronic and optical properties, these nanostructures are not only fundamentally interesting, but are currently considered to be likely candidates for components of future nanoscale devices. A hierarchical directed-assembly process, reminiscent of 'nanoLEGO', is expected to yield complex nanostructures for a large variety of purposes, ranging from microelectronics and sensors to unusual structural materials and medical applications.

The sub-nanometre size of the structures and the picosecond timescale associated with the processes leading to their formation are serious limitations to a direct observation of how these nanostructures form, and how they react on the atomic scale to mechanical stress or heat. Laws of quantum mechanics preclude us from directly observing the behaviour of electrons in fullerenes and nanotubes during photo-excitations, and in nanoscale electronic devices containing nanotubes of carbon and other materials. Not only the understanding of observed phenomena, but even more the prediction of unexpected behaviour, depends crucially on a proper theoretical description, often based on large-scale computer simulations.

This contribution will review areas where computer simulations have proven especially valuable, including prediction of the unusual mechanical and thermal stability of sp^2 bonded carbon nanostructures, microscopic processes underlying large-scale structural changes, and their thermal and electronic transport properties. The main objective here is not to provide an exhaustive review, but rather to illustrate the power of computer simulations in addressing a large variety of problems associated with carbon nanostructures.

2. Computational tools

Computer modelling allows us to understand the equilibrium geometry and electronic structure of nanoscale systems, and elucidates their formation process. Numerical simulations yield important information about the stability and chemical reactivity of particular nanostructures, as well as their response to mechanical, thermal, and electronic excitations. The computational tools addressing these questions span the entire range of techniques used in condensed matter and molecular physics, chemistry and engineering. Strain energy estimates based on continuum elasticity theory have proven useful to compare the relative stability of carbon cluster isomers, including fullerenes, onions, nanocones and nanotubes with single or multiple walls [5]. For predictive calculations of the electronic structure and total energy in the electronic ground state, the approach of choice is the *ab initio* density functional theory (DFT) within the local density approximation (LDA) [6, 7] or the generalized gradient approximation (GGA) [8]. The time evolution of the electronic states in an excited system is most often treated in the framework of the time-dependent density functional theory (TDDFT) within the TDLDA [9–11].

Atomic motion is determined using molecular dynamics (MD) simulations. The forces acting on atoms are obtained as gradients of the total energy, given within the DFT as a unique functional of the total charge density $\rho(\mathbf{r})$ as

$$E_{\text{tot}} = E_{\text{tot}}\{\rho(\mathbf{r})\}. \tag{1}$$

In the electronic ground state, $\rho(\mathbf{r})$ depends only on the ionic positions $\mathbf{R_i}$. The total energy expression (1) can be mapped onto a non-local band structure part, described by a parameterized linear combination of atomic orbitals (LCAO) Hamiltonian, and a remaining simple functional addressing inter-ionic repulsion [12]. Further separation into terms associated with individual atoms yields [13]

$$E_{\text{tot}} = \sum_i E_{\text{tot}}(i) = \sum_i E_{\text{bs}}(i) + \sum_i E_{\text{rep}}(i). \tag{2}$$

This total energy expression has proven very successful in total energy and molecular dynamics simulations of even large carbon nanostructures, since it is ideally suited for application on massively parallel vector computers for maximum speed-up.

In problems which involve sp^2 or sp^3 bonded carbon atoms only, and which do not attempt to describe breaking and formation of atomic bonds, the Tersoff bond-order potential [14, 15] has proven successful in describing total energy differences and elastic response of nanostructures.

In the electronically excited state, the charge density $\rho(\mathbf{r})$ also depends explicitly on time. Since the electron dynamics is typically two to three orders of magnitude faster than ion dynamics in bulk systems, most molecular dynamics simulations are performed within the Born–Oppenheimer approximation, assuming all electrons to be in the ground state irrespective of the atomic motion. Our recent finding of very long-lived electronic excitations in carbon nanostructures [16, 17] now imposes limits on the validity of Born–Oppenheimer dynamics, especially in processes involving electronic excitations.

3. Curious morphologies: function follows form

Interest in nanostructured carbon has been evolving steadily, as nanostructures other than fullerenes and nanotubes have been synthesized, often exhibiting unusual behaviour. On the nanometre scale, the equilibrium structure and also the physical characteristics of elemental carbon may change drastically. The resulting effects may be very different in nature, as illustrated in the following three examples. Due to the combination of a high speed of sound, hard optical vibration modes and a large phonon mean free path, carbon nanotubes prove to be the most efficient thermal conductors. The coupling of soft phonon modes to the macroscopic shape of nanotubes and fullerenes results in an unexpected thermal contraction behaviour. Particular carbon nanostructures, and heterostructured C/BN nanotubes, may acquire a net magnetic moment.

With their unique combination of physical properties, carbon nanostructures lend also themselves as functional building blocks of nanoscale devices. As will be discussed later, the proposed use of functionalized nanotubes ranges from a nanoscale counterpart of velcro fasteners to computer memory elements and chemical reaction vessels.

3.1. High thermal conductivity of nanotubes

With the continually decreasing size of electronic and micromechanical devices, there is an increasing interest in materials that conduct heat efficiently, thus preventing structural damage. The stiff sp^3 bonds, resulting in a high speed of sound, make monocrystalline diamond one of the best thermal conductors [18]. An unusually high thermal conductance should also be expected in carbon nanotubes [4, 19], which are held together by even stronger sp^2 bonds. These systems, consisting of seamless and atomically perfect graphitic cylinders a few nanometres in diameter, are self-supporting. The rigidity of nanotubes, combined with a virtual absence of atomic defects or coupling to soft phonon modes of the embedding medium, should make these systems very good candidates for efficient thermal conductors.

The expected high thermal conductivity value in nanotubes makes its direct experimental observation very difficult. Since thermal transport is likely to be dominated by phonon scattering in the contact region, the most important and currently unsolved challenge is to reproducibly create and characterize thermal contacts to a nanotube. Even if thermal scattering in the contact region could be minimized, the net thermal transport would still be limited by that of the leads. In view of these difficulties, predictive molecular dynamics calculations offer a viable alternative to direct measurements of thermal conductivity.

Such calculations, based on the Tersoff potential force field [14, 15] augmented by van der Waals interactions in graphite, have been performed for nanotubes and other carbon allotropes [20]. The results confirm that the thermal conductivity of isolated nanotubes equals or even surpasses that of isotopically pure diamond.

The thermal conductivity λ of a solid along a particular direction, taken here as the z axis, is related to the heat flowing down a long rod with a temperature gradient dT/dz by

$$\frac{1}{A}\frac{dQ}{dt} = -\lambda\frac{dT}{dz}, \tag{3}$$

where dQ is the energy transmitted across the area A in the time interval dt. In solids where the phonon contribution to the heat conductance dominates, λ is proportional to Cvl, the product of the heat capacity per unit volume C, the speed of sound v, and the phonon mean free path l. The latter quantity is limited by scattering from sample boundaries (related to grain sizes), point defects, and by umklapp processes. In the experiment, the strong dependence of the thermal conductivity λ on l translates into an unusual sensitivity to isotopic and other

atomic defects. This is best illustrated by the reported thermal conductivity values in the basal plane of graphite [21] which scatter by nearly two orders of magnitude. Similar uncertainties are likely to affect initial thermal conductivity measurements in 'mats' of nanotubes [22, 23].

In low-dimensional systems, such as nanotubes or graphene monolayers, we infer the volume from the way these systems pack in space (nanotubes form bundles and graphite forms a layered structure, both with an inter-wall separation of $\approx$3.4 Å) in order to the convert thermal conductance of a system to thermal conductivity of a material.

The attempt to determine λ using direct molecular dynamics calculations of an infinite nanotube with a superlattice of heating and cooling regions failed due to the large phonon mean free path of several hundred nanometres in nanotubes, requiring unit cells with up to 10^5 atoms. In smaller unit cells, we found that thermal conductivity was reduced by phonon scattering in the thermostat regions [20]. An alternate approach, based on the Green–Kubo formula for thermal conductivity [24] and equilibrium molecular dynamics simulations [25, 26], failed due to the slow convergence of the heat flux autocorrelation function.

The most suitable approach for calculating λ turned out to be an alternate approach [27] that combines the Green–Kubo formula with non-equilibrium thermodynamics [28, 29] in a computationally efficient manner [30]. In this approach, the thermal conductivity along the z axis is given by

$$\lambda = \lim_{\mathbf{F}_e \to 0} \lim_{t \to \infty} \frac{\langle J_z(\mathbf{F}_e, t) \rangle}{F_e T V}, \tag{4}$$

where T is the temperature of the sample, regulated by a Nosé–Hoover thermostat [31], and V is the volume of the sample. $J_z(\mathbf{F}_e, t)$ is the z component of the heat flux vector for a particular time t. $\mathbf{F}_e$ is a small fictitious 'thermal force' (with a dimension of inverse length) that is applied to individual atoms. This fictitious force $\mathbf{F}_e$ and the Nosé–Hoover thermostat impose an additional force $\Delta\mathbf{F}_i$ on each atom i. This additional force modifies the gradient of the potential energy and is given by

$$\Delta\mathbf{F}_i = \Delta e_i \mathbf{F}_e - \sum_{j(\neq i)} \mathbf{f}_{ij}(\mathbf{r}_{ij} \cdot \mathbf{F}_e) + \frac{1}{N} \sum_j \sum_{k(\neq j)} \mathbf{f}_{jk}(\mathbf{r}_{jk} \cdot \mathbf{F}_e) - \alpha\mathbf{p}_i. \tag{5}$$

Here, α is the Nosé–Hoover thermostat multiplier acting on the momentum $\mathbf{p}_i$ of atom i. α is calculated using the time integral of the difference between the instantaneous kinetic temperature T of the system and the heat bath temperature T_{eq}, from $\dot\alpha = (T - T_{\text{eq}})/Q$, where Q is the thermal inertia. The third term in equation (5) guarantees that the net force acting on the entire N-atom system vanishes.

Results for the thermal conductance of an isolated (10, 10) nanotube aligned along the z axis, based on non-equilibrium molecular dynamics simulations, are presented in figure 1. In this simulation, we used periodic boundary conditions with 400 atoms per unit cell. Each molecular dynamics run used for ensemble averaging consisted of 50 000 time steps of 5.0×10^{-16} s. Our results for the time dependence of $J_z(t)$ and $J_z(t)/T$ suggest that these quantities converge within the first few picoseconds to their limiting values for $t \to \infty$ in the temperature range below 400 K [20].

Results presented in figure 1 reflect the fact that λ is proportional to the heat capacity C and the phonon mean free path l. At low temperatures, l is nearly constant, and the temperature dependence of λ follows that of the specific heat. At high temperatures, where the specific heat is constant, λ decreases as the phonon mean free path becomes smaller due to umklapp processes. Our calculations suggest that at $T = 100$ K carbon nanotubes exhibit an unusually high thermal conductivity value of 37 000 W m^{-1} K^{-1}. This value lies very close to the highest thermal conductivity value ever observed, namely $\lambda = 41\,000$ W m^{-1} K^{-1}, which
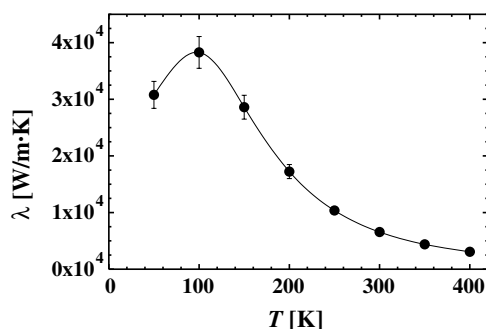
Figure 1. Temperature dependence of the thermal conductivity λ for a (10, 10) carbon nanotube for temperatures below 400 K. From [20], © American Physical Society.

has been reported [18] for a 99.9% pure ^{12}C crystal at 104 K. In spite of the decrease of λ above 100 K in nanotubes, the room temperature value of 6600 W m^{-1} K^{-1} is still very high, exceeding the reported thermal conductivity value of 3320 W m^{-1} K^{-1} for nearly isotopically pure diamond [32].

We found the thermal conductivity of nanotubes comparable in magnitude to that of a hypothetical isolated graphene monolayer. Our molecular dynamics simulations for the temperature dependent in-plane thermal conductivity of graphite, on the other hand, yielded values one order of magnitude lower, in good agreement with experimental data [33–35]. The plausible explanation for the large discrepancy between the thermal conductivity of a graphene monolayer and graphite is the inter-layer coupling in graphite, which reduces the phonon mean-free path. We should generally expect a similar reduction of the thermal conductivity for nanotubes in contact with other systems, including for nanotubes bundled to a rope, multi-wall nanotubes, and 'nanotube mats', also called 'bucky-paper'. Consistent with this conjecture is the low value of λ ≈ 0.7 W m^{-1} K^{-1} reported for bulk nanotube mats at room temperature [22, 23].

3.2. Thermal contraction of nanotubes

Carbon nanotubes are not only exceptional thermal conductors. As will be expanded upon below, their length also exhibits an unexpected behaviour, changing from an initial contraction to thermal expansion above 800 K [36]. Even though surprising at the first glance, we should point out that thermal contraction is quite common in low-dimensional systems, including polymers such as rubber or polyethylene [37, 38], layered systems such as graphite and boron nitride [39–41], and three-dimensional covalent networks found in oxides [42, 43] such as $NaTi_2P_3O_{12}$ and ZrW_2O_8.

Thermally induced shape changes result from competition between internal energy and entropy. In the harmonic regime at moderate temperatures, low-dimensional systems gain structural and vibrational entropy by exploring the voids in configurational space at relatively little energy cost. The dominating effect of entropy in this regime results in a contraction. Only at higher temperatures do the anharmonicities in the interatomic interaction play a significant role, causing an overall expansion. We expect the transition from contraction at low temperatures to expansion at high temperatures to be a universal phenomenon in low-dimensional materials, and only the crossover temperature to change from system to system. As we will discuss in the following, the interplay between energy and entropy has a particularly interesting effect on the thermal behaviour of nanotubes.

Here we use Nosé–Hoover molecular dynamics simulations [31, 44] to determine how temperature affects the volume of carbon nanotubes, and also to determine how their length changes with increasing temperature. We show that, at moderate temperatures, both fullerene molecules and carbon nanotubes contract in length and volume. Only at temperatures beyond several hundred degrees kelvin does the initial contraction change to an overall expansion in the anharmonic regime. We determine temperature-induced structural changes by investigating the coupling between vibrational modes and the shape of fullerenes and nanotubes. We identify those vibration modes that play a dominant role in how the volume and length of fullerenes and nanotubes change with temperature.

To correctly reproduce the change in length and volume of nanostructures in response to temperature, we need to describe precisely those energy changes associated with shape deformations in the anharmonic regime. We found that the popular Tersoff potential [14, 15] introduces a spurious soft mode that modifies the length of a straight tube, adversely affecting thermal expansion results [45, 46]. To avoid this problem, we performed molecular dynamics simulations based on the total energy functional of equation (2) [12]. This energy functional is particularly suited for our purpose, as it is based on an electronic Hamiltonian that goes well beyond the nearest neighbour approximation, thus also describing anharmonic effects due to the $sp^2 \rightarrow sp^3$ rehybridization during deformation. We focus on large structural changes occurring at hundreds of degrees kelvin, where classical description is adequate, and compare them to structures optimized at $T = 0$ K, ignoring the zero-point motion.

In the following, we report the effect of temperature on the length and volume of carbon nanotubes. Due to their natural abundance among single-wall carbon nanotubes grown by pulsed-laser vaporization [47], we focus on (10, 10) nanotubes[1] in our simulations. Also, nanotubes with a similar diameter are the most likely constituents of 'nanotube fleece' (or 'bucky-paper'), for which initial experimental measurements of thermal expansion have been performed [48]. We considered 50–1500 Å long open-ended segments of an isolated (10, 10) nanotube in order to calculate the effect of temperature on its volume and total length. The nanotube was coupled to a Nosé–Hoover thermostat in our canonical molecular dynamics simulations. Considering an open-ended segment rather than an infinite nanotube with periodic boundary conditions, we avoided introduction of spurious phonon modes and problems due to a fluctuating unit cell size. Since the vibrations of an open-ended segment are altered by the presence of under-coordinated carbon atoms, we ignored the five terminating layers[2] when evaluating the total length and volume of the tube segment.

Our results for the response of the nanotube to changing temperature are displayed in figure 2. The phonon modes, which couple most strongly to the nanotube length and volume, are illustrated in figures 2(e)–(h). The volume of a deformed nanotube can be estimated as a sum of partial volumes associated with each deformed layer, given by a product of its cross section area and the distance between adjacent layers. In a deformed nanotube segment, we first determine the centre of mass of the relevant layers and use the distance between them as the length. We approximate the cross-section area of each layer by that of a circle with radius r. This radius is given by the average distance of each atom from the centre of mass of that layer.

Data points representing the volume and length at a particular temperature have been obtained by taking a time average over 10^4–10^5 time steps of $\Delta t = 5 \times 10^{-16}$ s after

---

[1] Since the flexural rigidity of a graphene sheet is isotropic, thermal expansion of a nanotube should depend only on its diameter and not the chiral angle. The increased flexibility of nanotubes narrower than the (10, 10) tube is expected to augment the length contraction we find. Wider nanotubes, on the other hand, cannot bend easily, but show a tendency to collapse radially, augmenting the volumetric contraction.

[2] In achiral nanotubes aligned with the z axis, we define the ensemble of atoms with the same z coordinate as a 'layer'. In the (10, 10) nanotube, a layer consists of a 20 atom ring along the tube circumference.
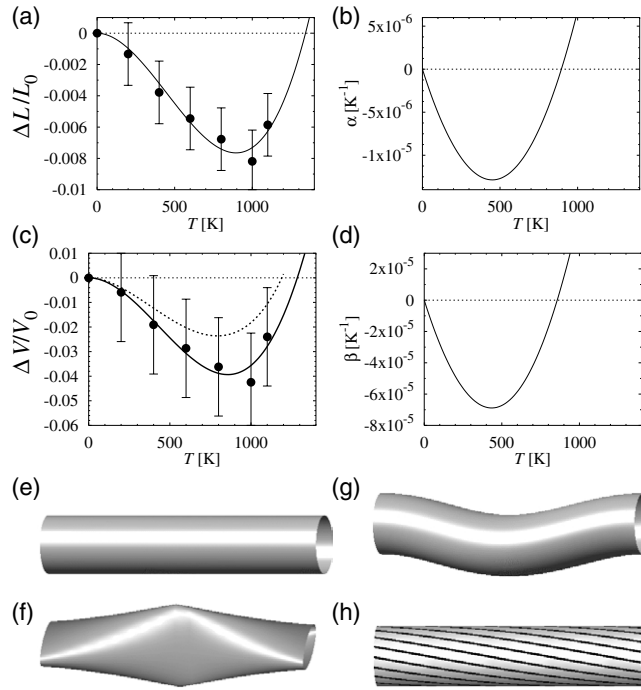
Figure 2. (a) Relative length change $\Delta L/L_0$ in a (10, 10) carbon nanotube as a function of temperature T. (b) Temperature dependence of the thermal linear expansion coefficient $\alpha = (1/L)(\mathrm{d}L/\mathrm{d}T)$. (c) Relative volume change $\Delta V/V_0$ and (d) thermal volumetric expansion coefficient $\beta = (1/V)(\mathrm{d}V/\mathrm{d}T)$ of the (10, 10) nanotube as a function of temperature. Schematic snapshots of selected soft phonon modes that couple strongly to the length and volume of the nanotube: (e) reference structure of the unperturbed tube, (f) optical pinch mode, (g) transverse acoustic bending mode, (h) twist mode. The relative contribution of the pinch mode to the volume change is shown by the dashed line in (c). From [36], © American Physical Society.

equilibration with the heat bath. We have filtered out high-frequency noise using a simplified Fourier analysis of the total volume and length as a function of time at 200, 400, 800, 1000 and 1100 K. The error bars reflect the additional uncertainty associated with this fitting process.

Our results for the temperature dependence of the tube length, shown in figure 2(a), suggest that carbon nanotubes should contract up to very high temperatures close to 1300 K. These findings are in agreement with the observed contraction in 'bucky-paper' below room temperature [48]. The solid curve is a fit to the same functional form as used in the thermal expansion analysis of graphite [49], which also shows an in-plane contraction at low temperatures.

The linear thermal expansion coefficient α is defined as

$$\alpha = \frac{1}{L}\frac{\mathrm{d}L}{\mathrm{d}T}. \tag{6}$$

Molecular dynamics simulations for the (10, 10) nanotube suggest that α decreases from its initial zero value at $T = 0$ K, and becomes negative. The minimum value in the $\alpha(T)$ curve, corresponding to the maximum thermal contraction, is $\alpha \approx -1.2 \times 10^{-5}$ K^{-1} and occurs at $T \approx 400$ K. This is significantly larger than the in-plane graphite value of -1.3×10^{-6} K^{-1} at 300 K [39], and comparable to the polyethylene value of -0.8×10^{-5} K^{-1} at 200 K [38]. Contraction continues up to $T \approx 800$ K, where α vanishes and the tube length is minimum.

Above 800 K, α becomes positive, indicating onset of thermal expansion, as the anharmonic part of the inter-atomic potential gains in importance. Above 1300 K, the tube should exceed its initial length at $T = 0$ K.

Since the above finding of a temperature dependent thermal expansion coefficient contradicts the prediction of a temperature independent value of α, based on the Grüneisen theory [50], within the classical regime below the Debye temperature, our neglect of quantum effects in this temperature range needs to be justified.

The vibration spectrum of sp^2 bonded carbon nanostructures is dominated by hard optical modes, associated with the distortion of the interatomic bonds, and by rather soft, long-wavelength acoustic modes, many of which couple to the global crystal shape. The interatomic bonds in sp^2 and sp^3 bonded carbons are similarly stiff, resulting in a formidable Debye temperature of 1860 K in diamond [50]. The long-wavelength, soft acoustic modes give rise to lower Debye temperatures, ranging from 420 K in graphite [51] down to $\approx$30 K in nanotubes [52]. Whereas a classical description of the soft transverse acoustic modes, depicted in figure 2, appears appropriate above room temperature, the classical description of the hard optical modes needs to be justified.

Unlike the soft transverse acoustic modes, which cause a length contraction in nanotubes and graphene monolayers even in the harmonic regime [36], the hard optical modes do not cause macroscopic length changes in the harmonic regime, whether subject to the Bose–Einstein or the Maxwell–Boltzmann statistics. In other words, the classical treatment of these modes does not affect results for $\alpha(T)$. Only at temperatures $T \gtrsim 800$ K does the increasing importance of higher-order anharmonicities in the C–C interaction, which are not considered in the Grüneisen theory, eventually dominate over the contraction caused in nanotubes by transverse acoustic modes.

Having justified the neglect of quantum effects in the molecular dynamics simulation, we should also emphasize the advantages of classical MD simulations over a classical statistics approach in determining $\alpha(T)$ at finite temperatures. In our classical MD simulation, the amplitude of individual vibration modes is determined by Newton's laws and accurate force fields. This amplitude is generally large for soft modes and small for hard modes at a given temperature, qualitatively following the behaviour of a quantum crystal. The equipartition theorem of classical statistics, which postulates equal population of all modes independent of temperature, is expected to describe structural changes at finite temperatures much less accurately.

In order to understand the origin of thermal contraction, we analysed our molecular dynamics simulations in terms of normal vibration modes that couple strongly to the length and volume. In the harmonic regime, there is no change to the bond lengths and the area. Shape changes, resulting from area conserving tube deformations, reduce the mean tube radius and lead to a volumetric contraction. We focused on the soft modes that do not change the surface area of the reference tube, shown in figure 2(e). The significant modes are the pinch mode, the bending mode and the twist mode, depicted in figures 2(f)–(h), respectively. Whereas short-wavelength modes, such as the pinch mode, can be described in our atomistic molecular dynamics simulations, description of long-wavelength modes requires long tube segments exceeding our computational resources. To describe the long-wavelength bending and twisting phonon modes, we performed molecular dynamics simulations based on a model assumption of rigid atomic layers that interact according to the energy functional described above.

Our long-wavelength calculations suggest that the transverse acoustic bending mode, depicted in figure 2(g), is very soft, as it involves a shear motion that requires a minimum of bond stretching and bending. Our simulations indicate that length contraction due to this mode saturates in (10, 10) tube segments with a length close to 100 Å. We find the bending mode

to contribute almost one third towards the length contraction of a (10, 10) nanotube. Also the soft twisting mode, depicted in figure 2(h), can be viewed as a shear mode. We found this mode to be active in the orientational melting within a nanotube rope at low temperatures [53], and to contribute up to $\approx 10\%$ towards the tube length contraction. Since none of these modes affects the tube cross-section, their effect on the volumetric contraction is very small.

Our calculations suggest that an important contribution towards the longitudinal contraction, and the dominant contribution towards the volumetric contraction, comes from the optical 'pinch' mode, shown in figure 2(f). The dashed curve in figure 2(c) indicates the analytically calculated[3] contribution of a pure pinch phonon mode to the total volume change. We find that the pinch mode accounts for nearly one half of the volume change, but only one third of the total length change.

3.3. Magnetism in foams and heterostructured nanotubes

Electronic structure results for fullerenes and nanotubes suggest that even minute changes in the spatial arrangement of carbon atoms can profoundly alter the electronic properties of these systems from a semiconductor to a metal or superconductor [54–57]. One could expect that structural rearrangements might also significantly change the magnetic properties of all-carbon allotropes from their known diamagnetic behaviour [58, 59].

Only recently a weakly magnetic all-carbon structure has been reported, formed under high-pressure and high-temperature conditions, consisting of rhombohedrally polymerized C_{60} molecules [58]. Other experimental observations suggest the occurrence of ferromagnetism in a semiconducting nanostructured carbon foam with a low mass density [60]. As will be shown in the following, the unexpected magnetic behaviour of all-carbon systems can be quantitatively interpreted using spin-polarized *ab initio* calculations. Our results suggest that unpaired spins are introduced by sterically protected carbon radicals, which are immobilized in the non-alternant aromatic system of sp^2 bonded carbon with negative Gaussian curvature. This new mechanism to generate unpaired spins in semiconductors may find a useful application in the emerging field of spintronics.

Here we focus on the electronic and magnetic properties of an sp^2 bonded four-nanotube junction, which is structurally related to schwarzite [61–64]. This all-carbon system, depicted in figure 3(a), is a possible building block of the recently synthesized nanostructured carbon foam [60, 65, 66]. The most striking finding here is that of a magnetic ground state. We find the origin of magnetism in this system to be different from previous reports [67, 68], which related the spin polarization at a graphite edge to the presence of under-coordinated carbon atoms. Our calculations suggest that unpaired spins may also be introduced by carbon radicals, and not only by under-coordinated carbon atoms.

Our electronic and magnetic structure calculations are based on the 'tetrapod' geometry shown in figure 3(a). The core, depicted in figure 3(b), consists of the warped sp^2 bonded building block of the 'plumber's nightmare' structure [62]. It is formed by a network of hexagons and heptagons only, and is connected to four (9, 0) nanotube extremities. Depending on the degree of hydrogen passivation, the exposed nanotube edges are terminated by sp^2 or

---

[3] Each tube layer in the pinch mode is subject to an elliptical deformation. To calculate the volumetric contraction in this mode, we assumed the circumference C of the elliptical cross-section to be constant. In this case, the area S of the ellipse decreases monotonically with increasing eccentricity $t \equiv b/a$, defined as the ratio of its major and minor axes a and b. Making use of the complete elliptic integral of the second kind $E(x)$, the ellipse area is given by $S(t) = (\pi C^2/16)(t/[E(1-t^2)]^2)$. Assuming that t changes linearly between t_{min} and 1 along the axial direction, the total volume V of the deformed nanotube segment of length L changes as $V = \int_0^L \mathrm{d}l \, S(t) = L\langle S \rangle$, where $\langle S \rangle = \int_{t_{min}}^1 \mathrm{d}t \, S(t)/(1 - t_{min})$.
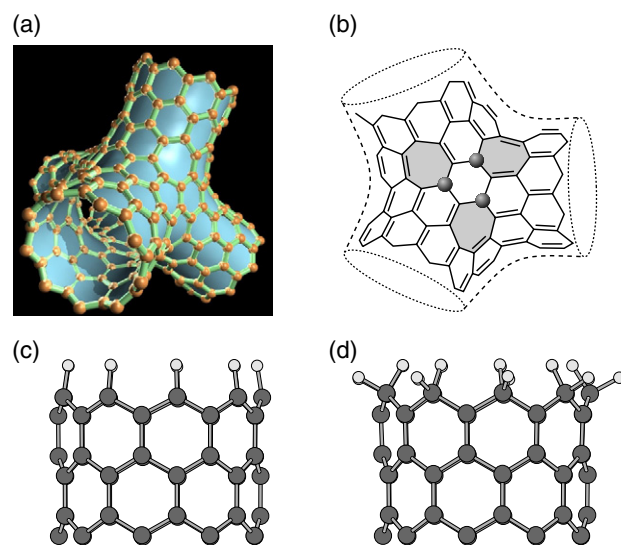
Figure 3. (a) The structure of a carbon tetrapod, a possible building block of schwarzite. The four extremities consist of (9, 0) nanotubes with a zigzag edge. (b) Introduction of trivalent carbon radicals, emphasized by the grey spheres, in the aromatic system of the otherwise tetravalent carbon atoms in the tetrapod core. The radicals are associated with heptagons, indicated by grey shading. The structure of an (c) sp^2- and (d) sp^3-terminated (9, 0) nanotube, with the smaller spheres indicating the hydrogen atoms. From [59], © American Physical Society.

sp^3 carbon atoms [69]. In this type of schwarzite-related structure, tubular segments of zero Gaussian curvature coexist with saddle-like regions of negative Gaussian curvature. We expect that a range of schwarzite-like building blocks similar to this could be cross-linked to form a foam structure with a very low mass density, which carries a magnetic moment.

The electronic structure of different tetrapods is calculated using the density functional theory within the local spin density approximation (LSDA), employing the Ceperley–Alder exchange–correlation functional for the local spin density [70, 71] and *ab initio* pseudopotentials [72, 73]. To facilitate the numerical treatment of very large aggregates containing hundreds of atoms within LSDA, we make use of our recently developed approach based on an atom-centred numerical basis set [74], proven to describe correctly similar carbon systems [75]. We use Pulay corrections [76] to the Hellman–Feynman forces during structure optimization.

To discriminate between the effect of the sp^2 core region and the edge region in our magnetic structure calculations, we have considered hydrogen terminated C_{264} and C_{336} clusters with the same core structure, but a different length of the nanotube extremities. We assume that the edge of these extremities may be terminated in three different ways. Besides the bare, unterminated edge, we consider an sp^2 termination by one hydrogen atom per edge atom, shown in figure 3(c). In the sp^3 terminated structure shown in figure 3(d), each carbon edge atom is connected to two hydrogen atoms. The interface between the sp^3 edge atoms and the sp^2 atoms of the nanotube is analogous to that found in diamond–graphite hybrid structures [77]. In the following, we disregard structures with a bare edge, since they are likely to be passivated quickly under experimental conditions due to their high reactivity.

The electronic structure of the tetrapod is presented in figure 4. The projection of the total density of states onto the 192 carbon atoms in the core region, including twelve heptagon
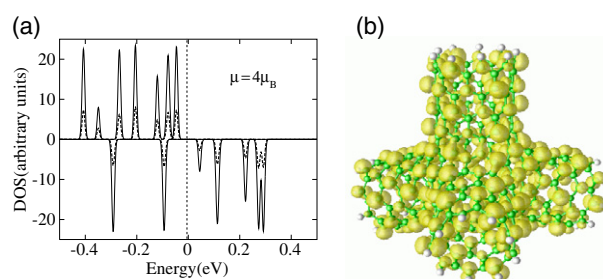
Figure 4. Electronic structure of the sp^3 terminated C_{264} tetrapod shown in figure 3(a). (a) Spin-resolved electronic density of states, with the majority spins shown in the upper panel and the minority spins in the lower panel. The Fermi level lies at $E = 0$. The solid curve represents the projection of the density of states onto the 192 core carbon atoms. The dashed curve represents that of the 72 carbon atoms at the zigzag edges. The discrete level spectrum has been convoluted with a Gaussian with a full width at half maximum of 0.012 eV. (b) Charge density associated with the four unpaired electrons close to the Fermi level. From [59], © American Physical Society.

rings, is shown by the solid curve, and that of the 72 atoms at the edges by the dashed curve. We focus on a 1 eV wide energy window around the Fermi level, which determines the magnetic behaviour, since electrons with higher binding energies are all paired. Artificial level broadening was used only in the figure, for the sake of visual clarity; no broadening has been applied during the self-consistent calculations.

Our calculations indicate the presence of twelve unpaired spins in an sp^2-terminated tetrapod. Further decomposition of the density of states suggests that eight of the twelve spins are strongly localized at the zigzag edges, with two unpaired spins at each edge, and the remaining four are associated with the core. The density of states of an sp^3-terminated tetrapod, depicted in figure 4(a), suggests the presence of four unpaired spins, all of them associated with the core of the system. A detailed analysis revealed that the electronic states associated with the majority spin are not localized, but rather spread out across the entire cluster, as shown in figure 4(b). We found that the exchange splitting of the four states decreases with increasing nanotube length. This can be understood in terms of the exchange interaction between two electrons, which occupy the same region. The origin of the exchange splitting is the Coulomb repulsion between these electrons, which decreases as the region grows.

These findings raise several intriguing questions. The first important question is, what distinguishes the magnetic structure, shown in figure 3(a), from other carbon structures, which are non-magnetic, or systems, where magnetism arises due to under-coordinated edge atoms? Equally important is to find the reason for the occurrence of the spin polarization and its apparent robustness with respect to selected structural changes.

In our calculations for tetrapods terminated in different ways, we found the number of unpaired spins not to be affected by changing size and boundary shape of the tetrapod, but to depend sensitively on the bonding topology. Setting aside the role of unsaturated graphitic edges in magnetism, which has been discussed before [67–69], we found the presence of higher polygons, introducing a negative Gaussian curvature, to be a necessary condition for a magnetic ground state. To investigate a possible conjecture that negative curvature is also a sufficient condition to establish spin polarization, we calculated the electronic ground state of a tetrapod, where all four extremities were terminated by C_{60}-derived caps. Our finding of an energy gap of 0.34 eV between the highest occupied and the lowest unoccupied state in this structure, which excludes the possibility of a Fermi instability, proved this conjecture incorrect.

The only viable explanation for the occurrence of magnetism in an all-carbon structure is the introduction and stabilization of carbon radicals. The occurrence of radicals, which can introduce an unpaired spin, is directly related to the possibility of pairing all valence electrons in covalent bonds. No radicals should be expected to occur if bonds in the system can be assigned in a way that would keep all carbon atoms tetravalent. In a graphitic structure, each tetravalent carbon atom is connected to three neighbours by one double and two single bonds. In such a case, all electrons should be paired and the structure should be diamagnetic. This is the case in C_{60} and other fullerenes, where all carbon atoms are kept tetravalent by associating single bonds with the edges of pentagons. Also in a planar graphene sheet or an infinite nanotube, all carbon atoms are equivalent and tetravalent.

Failure to find a global bonding scheme, where each carbon atom is associated with one double and two single bonds, leads to the introduction of radicals due to a frustration in the electronic system. As we expand on below, this is the case in the tetrapod structure of figure 3(a), where twelve trivalent carbon radicals are introduced as a consequence of inserting twelve heptagons in the otherwise alternant aromatic system of the graphitic honeycomb lattice. These trivalent carbons, emphasized in figure 3(b) by the grey spheres, are the source of spin polarization. In the structure discussed here, these radicals are sterically protected within the system of 'single' and 'double' bonds imposed by the tetrapod topology, and occur in groups of three.

This conclusion can be reached by analysing the bonding scheme in the sp^3 terminated tetrapod. The system of single and double bonds shown in figure 3(b) follows the bonding at the edge of the terminating nanotube. Since two valence electrons of the terminating carbon atoms are paired with those of hydrogen, all bonds along the zigzag edge must be single bonds. To keep carbon atoms at the edge tetravalent, adjacent bonds in the axial direction must be double bonds, as shown in figure 3(b). Following this scheme into the core region of the structure necessarily leads to the above mentioned frustration, which leaves several sites, namely the trivalent carbon radicals with a lone electron, connected to their neighbours by only three single bonds.

The lone electrons need not be localized at the radical sites, but rather gain energy by delocalizing across the entire structure, as shown in figure 4(b). We find the radicals to form groups of three in the tetrapods. Assuming that two of the three spins are paired, each group of three radicals should contribute one unpaired spin to the structure. With four groups of radicals per tetrapod, we would expect four unpaired spins in total, in agreement with our spin density functional calculation.

Stabilization of carbon radicals by steric protection has been known since the synthesis of triphenylmethyl in 1900 by Gomberg [78]. Radicals such as perinaphthenyl (or phenalenyl) have even been investigated as potential molecular conductors by Haddon [79]. Whereas sterically unshielded carbon-based radicals have been reported recently in organic systems [80], our study is the first report to our knowledge that identifies carbon radicals in an undoped all-carbon structure with no apparent exposed edges. We should emphasize that the magnetism found in this study is caused by the presence of sterically protected radicals within nanometre-sized conducting segments of sp^2 carbon. It could also occur in other nanostructured solids, which may be different from the tetrapod structure discussed here. We believe this to be a general phenomenon, the discovery of which may strongly influence the emerging field of spintronics.

3.4. Nanotube hooks as nanovelcro

The extraordinary mechanical properties of carbon nanotubes [4], including their high stiffness [81–83] and axial strength [84, 85], are related to the unparalleled tensile strength of graphite [49]. In single-wall nanotubes [86, 87], substitution of hexagons by pentagon–heptagon pairs is known to cause a permanent bend in the tube and to change its chirality [88].
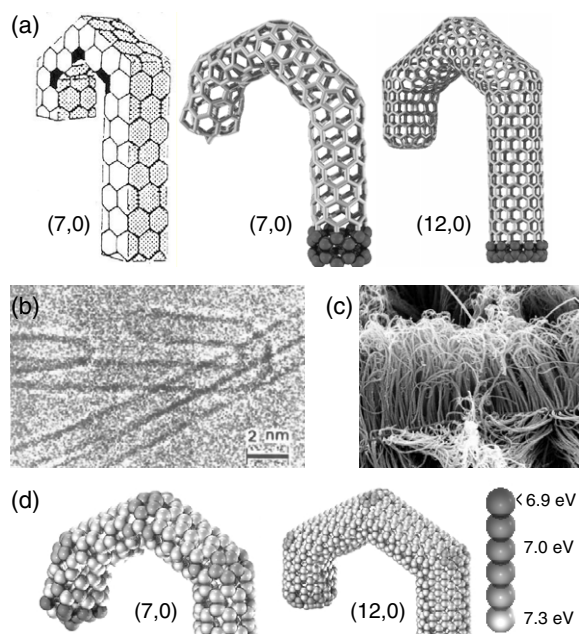
Figure 5. Structure of a nanotube-based hook. (a) Schematic view of a hook, formed by inserting pentagon–heptagon pairs in an all-hexagon tubular structure, and the equilibrium structure of hooks based on a (7, 0) and a (12, 0) nanotube. (b) Transmission electron micrograph of a nanotube-based hook, published in [89]. (c) Scanning electron micrograph of an array of nanohooks grown on a surface [90]. (d) Atomic binding energies in (7, 0) and (12, 0) nanohooks. The grey scale coding reflects the energy scale on the right. From [93], © American Physical Society.

The morphology of a nanotube deformed to a hook is illustrated schematically in figure 5(a). A high-resolution transmission electron micrograph (HRTEM) of this system [89] is reproduced in figure 5(b), and a scanning electron micrograph (SEM) of nanohooks [90] is shown in figure 5(c). So far, studies of nanotubes containing pentagon–heptagon pairs have concentrated on their intriguing electronic properties [91, 92].

As will be discussed in the following, nanotube-based hooks or related structures may effectuate bonding between solid surfaces [94], as a nanometre-scale counterpart of velcro. We study the physical properties, including mechanical strength and resilience, of a micro-fastening system consisting of solid surfaces covered with nanohooks, illustrated in figures 6(a) and 5(c), which we call 'nanovelcro'. By studying the atomic-scale processes during closure and opening, we show that a nanovelcro junction should be ductile rather than brittle, and exhibit large toughness. We find that nanovelcro offers significant advantages over conventional adhesives and welding, including thermal stability to 4000 K, and a self-repair mechanism under local shear. With a large density of hooks per area, strong bonding can be achieved in parallel to mechanically decoupling the connected parts.

To determine the physical behaviour of the nanovelcro micro-fastening system, we combine total energy and structure optimization calculations with molecular dynamics simulations. In order to describe realistically a possible $sp^2 \rightarrow sp^3$ rehybridization during the opening and closing of nanovelcro bonds, we use the total energy functional of equation (2) [12]. When modelling the dynamical processes during opening and closure of the hook assembly in figure 6(a), we subject the grey-shaded rigid anchor sections to either a constant force or a constant velocity in the desired direction.
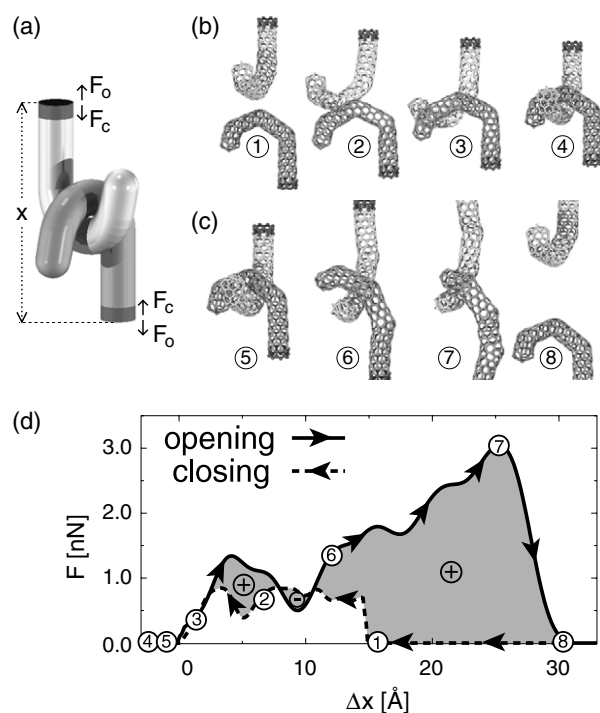
Figure 6. (a) Schematic drawing of a two-hook assembly, defining the anchor distance x, the direction of the opening force F_o and the closing force F_c. Snapshots of the $(7, 0)$ nanohooks during (b) closure and (c) opening of the nanohook assembly. (d) Force acting on the nanohooks during the opening and closure of the assembly as a function of the relative anchor displacement Δx. The labels correspond to structures depicted in (b) and (c). The grey-shaded area, depicting the hysteresis, represents the energy dissipated during an opening–closing cycle. From [93], © American Physical Society.

As illustrated in figure 5(a), a set of six pentagon–heptagon pairs causes a permanent deformation of a $(7, 0)$ single-wall nanotube to a nanohook [89]. Euler's theorem suggests that a hook deformation due to pentagon–heptagon insertion does not depend on the chiral index of the tube. This is illustrated by comparing the relaxed structures of the $(7, 0)$ and the wider $(12, 0)$ nanotube in the right panel of figure 5(a). Even though substitution of hexagons by pentagon–heptagon pairs in a nanotube is energetically unfavourable, the system is sufficiently flexible to redistribute the strain in the vicinity of the pentagons and heptagons.

To visualize this strain redistribution in the structure, we grey-shaded the spheres representing individual atoms according to their binding energy in figure 5(d). We found all the atomic binding energies to be lower than the 7.4 eV value of graphite. The least stable atoms, indicated by the darkest shading in figure 5(d), are located in the caps. The atomic arrangement at the hemisphere terminating the $(7, 0)$ nanotube is similar to the strain in the C_{24} fullerene, with atomic binding energies of only ≈ 6.4 eV. The cap structure at the end of the $(12, 0)$ nanotube resembles that of the more stable C_{84} fullerene, with atomic binding energies close to 7.1 eV. In general, we expect the occurrence of pentagon–heptagon defects, causing the permanently bent structures shown in figures 5(b) and (c), primarily at lower synthesis temperatures, where such defects cannot be annealed easily [89, 90].

A pair of mating nanohooks is illustrated schematically in figure 6(a), together with the direction of the opening force F_o and the closing force F_c. The nanohooks are to be considered

permanently anchored in the surfaces to be connected. The anchor regions are emphasized by the dark colour and separated by the distance x. The forces are given by the gradients for the total energy of the nanohook structure with the exception of the rigid edge regions, emphasized by the dark colour in figures 5(a) and 6(a)–(c). Snapshots of the (7, 0) nanohook engagement process are shown in figure 6(b). In spite of significant structural deformations during this transition, we found no signs of irreversibility associated with a possible local $sp^2 \rightarrow sp^3$ transition or a permanent structural change, reflecting the resilience of the nanohooks to mechanical deformations.

In our molecular dynamics simulation, we subject the anchor region of the hooks to a constant velocity $v_c = 25$ m s^{-1} and monitored the force F_c during the closure process. Comparing results for different velocities, we found the force $F_c(x, v_c)$ to depend only on the relative distance x between the anchor regions at low displacement velocities. Our results indicate that the value of $F_c(x)$, based on molecular dynamics simulations, agrees with results based on static structure optimization with constrained anchor regions. At velocities $v_c \gtrsim 75$ m s^{-1} we observed an increase in $F_c(x, v_c)$ due to the inertia of the nanostructure. For the sake of convenience, we defined $x = x_0 + \Delta x$, where x_0 is the shortest distance between the anchor regions, at which the substructures started interacting. Numerical results for $F_c(\Delta x)$, displayed by the dashed line in figure 6(d), indicate that closure of the (7, 0) nanohook assembly requires an average force of $\langle F_c \rangle \approx 0.9$ nN.

The dynamics of the opening process is illustrated by the snapshots in figure 6(c). As during the closing process, we subjected the anchor regions of the hooks to a low constant velocity $v_o = 25$ m s^{-1} and monitored the force F_o during the opening process. The results, given by the solid curve in figure 6(d), indicate an average opening force of $\langle F_o \rangle \approx 1.7$ nN, about twice the value of the closing force. The opening force increases as the hook becomes stiffer while stretched, and reaches the maximum value of $F_o \approx 3.0$ nN. In spite of this considerable force, we have not observed any irreversible structural changes in the nanohook assembly, including the least stable terminating cap. Even in the most strained structure ⑦ in figure 6(c), the closest inter-wall distance between the hook substructures was in excess of 2.1 Å, thus preventing a local $sp^2 \rightarrow sp^3$ rebonding [95].

When exploring the suitability of nanohooks for bonding, we assume that the nanohooks are permanently anchored in the substrate by covalent bonds. These bonds are particularly strong for nanohooks grown on diamond, metals and carbides. Uprooting the hook would require a very high force, possibly comparable to the average force of ≈50 nN associated with cleaving the tube axially described below. The forces needed to open and close the nanovelcro bond are much smaller and will not detach the hook assembly from the anchor points.

To determine which parts of the nanohook assembly are most prone to damage, we monitored the distribution of bond lengths and atomic binding energies during the opening process. Even in the most strained structure ⑦, we observed a maximum bond length increase of ≈0.05 Å beyond the graphite value $d_{CC} = 1.42$ Å, found in the initial structure ⑤. We found the distortion to be accommodated by a large portion of the system, reflecting the ductility of the bond. These findings, together with the structural snapshots shown in figures 6(b) and (c), confirm that nanovelcro maintains its structural integrity during repeated opening and closing.

Our results in figure 6(d) also provide quantitative information about the toughness of the (7, 0) nanovelcro bond, defined as the energy needed to open the nanohook assembly. The calculated toughness of ≈30 eV is very high, almost twice the energy investment of 15.4 eV to cleave a perfect (7, 0) nanotube. The simple reason for this unexpected result is that an average opening force $\langle F_o \rangle \approx 1.7$ nN, acting over a large distance of 30 Å, performs more work than the much higher force of ≈50 nN, which cleaves axial bonds across a distance of 0.5 Å. Upon opening, the energy stored in the strained hook structure is deposited into the internal degrees

of freedom, heating up the nanostructure locally. This energy is efficiently carried away due to the excellent thermal conductivity of carbon nanotubes [20], thus preventing irreversible structural changes.

Next, we define the stability of the nanovelcro bond as the energy to close and reopen the nanohook assembly, given by $\Delta E_b = \int_{-\infty}^{\infty} (F_o(x) - F_c(x))\,\mathrm{d}x$. We find a large value of $\Delta E_b \approx 24$ eV for the stability of the $(7, 0)$ nanohook system, corresponding to the shaded area in figure 6(d). The relatively small difference between the toughness and the stability of the bond is due to the low amount of energy required to close the hook, given by the area under the dotted line.

It should be emphasized that the crucial feature of the nanovelcro bond is not the shape of the deformed nanotubes, but rather the area under the force-displacement hysteresis curve in figure 6(d). Other structures, including coils [96–98], can be combined with hooks and other deformed tubes for efficient bonding. The ability of hooks to open and close reversibly furthermore results in a unique self-repairing capability. This is of particular interest when bonding solids with different thermal expansion, such as applying a diamond coating to metals, since self-repair should prevent delamination in the case of large temperature fluctuations.

The usefulness of nanovelcro for permanent bonding becomes particularly obvious when considering two flat solid surfaces covered by an array of nanohooks. In view of the small nanohook cross-section, we may find up to one nanohook per nm^2, corresponding to an ideal coverage of 10^{18} nanohooks m^2. Thus, detachment of nanovelcro bonded areas should require an energy investment of $\lesssim 5$ J m^{-2}. This is significantly more than the energy to cleave most crystals, which is twice their surface energy, and is responsible for the unusual toughness of the nanovelcro bond. In view of the large force required to open a nanohook assembly, the ultimate strength of 'ideal' nanovelcro should lie close to 3 GPa, more than in most solids[4]. Under tensile load, we expect the solids to break first, while the nanovelcro bonds remain engaged.

3.5. Nanotube peapods: nanoscale memory and beyond

A new type of self-assembled hybrid structures called 'nanopeapods', consisting of fullerene arrays inside single-wall carbon nanotubes, have recently been reported [99–103]. Potential uses of nanopeapods range from nanometre-sized containers [102] to data storage [104], and possibly high-temperature superconductors [105]. The demonstrated ease of fullerene peapod formation suggests the possibility of also encapsulating other nanostructures, including diamondoids [106], and possibly even polymers, such as polyacetylene [107].

The encapsulation of a fullerene in a nanotube is associated with a sub electron-volt energy gain across a sub-nanometre distance, the size of the fullerene. This translates into an average force of nanonewtons, which pulls fullerenes into the nanotube. Similar forces occur during central collisions between encapsulated fullerenes even at room temperature. Dividing nanoNewton forces by the cross-section area of a nanotube, of the order of nm^2, translates into a formidable pressure of GPa. In other words, a peapod may also be considered a nanoscale autoclave, which can facilitate selective chemical reactions, including a fusion of encapsulated fullerenes [108].

3.5.1. Formation of nanotube peapods.
Even though the encapsulation of fullerenes (such as C_{60}) in nanotubes is favourable on energetic grounds [104, 109, 110] and occurs rapidly by

---

[4] In reality, the hook packing density and registry are likely to be worse than the ideal case, thus reducing the effective ultimate strength.

exposing nanotubes to sublimed fullerenes [99–103], virtually nothing is known about how the fullerenes enter the nanotubes when forming the nanopeapods.

A statistical mechanics approach, which considers only the initial and final state, describes only the equilibrium state after an infinite time [110]. It can say nothing about the likelihood of fullerene encapsulation in a finite time, as it ignores any activation barriers along the reaction path. Only trajectory calculations based on the complex potential energy surface of the system, such as those of [111], can provide detailed answers about the dynamics and intermediate steps involved in the formation of nanopeapods.

An important controversy involves the question of whether fullerenes enter through the open ends of perfect nanotubes, or whether defects in the wall play an important role as entry channels. The extremely high filling ratio of up to 100% [103] appears hard to achieve even within a few days if the only entry channels are the two open ends of each tube. In such a case, the fullerene kinetics is limited and even a single impurity may block an entry channel. On the other hand, only few openings in the tube walls have been observed in high-resolution transmission electron microscopy (HRTEM) images [112]. Another important question, which a statistical approach cannot answer, is whether the encapsulation process, be it through an open end or through a defect, occurs directly from the gas phase, or involves a diffusive motion along the wall.

In the following, we discuss results of a large-scale simulation for the entry of a C_{60} molecule into a (10, 10) carbon nanotube via different scenarios, illustrated in figure 7. We consider the encapsulation through the open end of a free-standing nanotube (figure 7(a)) and through the open end of a nanotube bundle (figure 7(b)). These scenarios are compared to the C_{60} entry through a defect, in our model a large opening in the nanotube wall (figure 7(c))[5]. Formation of such large defects may occur, we believe, during the harsh purification process that is a necessary prerequisite for peapod formation [102]. By assuming that the C_{60} adsorbs on the wall prior to encapsulation, we take advantage of the enhanced probability of the fullerene finding an entry channel into a nanotube within the lower-dimensional phase space probed by the C_{60} diffusing along the wall, as compared to a fullerene in the gas phase. The molecular dynamics simulations elucidate not only which of these processes is most likely, but also the optimum temperature window for the peapod formation.

The potential energy of the fullerene–nanotube system is evaluated using the total energy functional of equation (2) [12]. This approach describes accurately not only the covalent bonding within the graphitic substructures, but also the modification of the fullerene–nanotube interaction due to the inter-wall interaction and possibly the presence of unsaturated bonds at defect sites or tube edges[6]. We find the use of an electronic Hamiltonian to be required in this system, as analytical bond-order potentials do not describe the rehybridization at defect sites and tube ends with a sufficient precision. Once the quantum nature of the interatomic interactions has been taken into account, the trajectories of the heavy carbon atoms are described reliably in classical manner.

In figure 7 we present schematic views of the encapsulation scenarios together with the calculated potential energy surfaces in the $x-y$ plane that contains the tube axes, the centre of the C_{60} molecule and the defect. The tube structures underlying the potential energy surfaces have been globally optimized. They reflect the relaxation at the open end of the tube and the

---

[5] We propose that what has been interpreted as harmless 'amorphous overcoating' of perfect single-wall nanotubes in HRTEM images may indeed represent defective nanotube segments with openings large enough to let a fullerene pass through.
[6] Due to their enhanced reactivity, unsaturated edges form a stronger bond with the fullerenes than edges saturated with hydrogen or other elements. It is conceivable that fullerenes could get trapped near vacancies that are smaller or comparable in size with the fullerene.
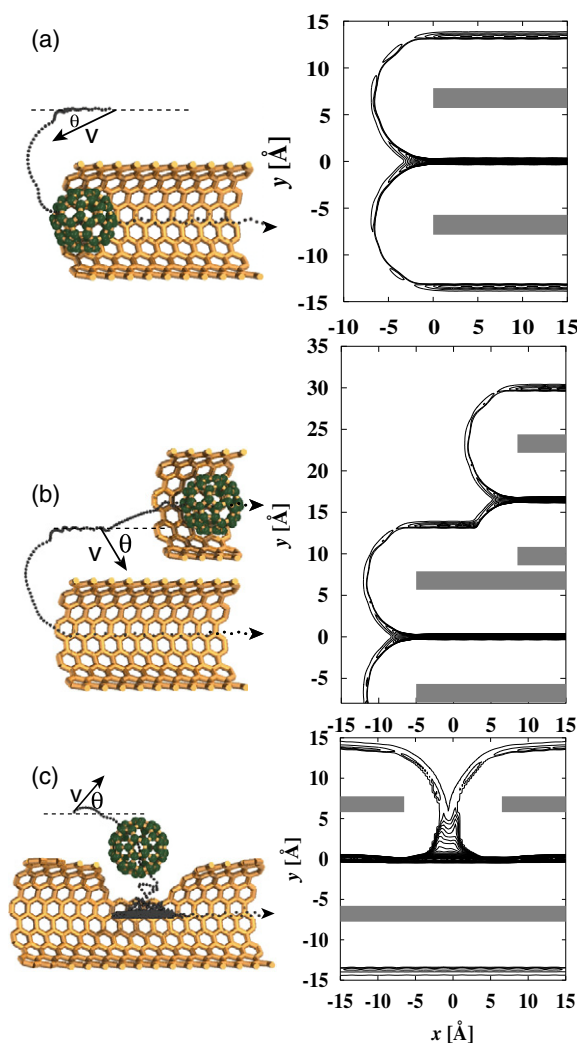
Figure 7. Perspective views (left panels) and potential energy surfaces (right panels) for the encapsulation of a C_{60} molecule in a $(10, 10)$ nanotube under different scenarios. Dotted lines indicate possible C_{60} trajectories, characterized by the launch velocity v and launch angle θ with respect to the tube axis. The potential energy surfaces are shown in the $x-y$ plane containing the centre of the fullerene and the tube axis x. Adjacent energy contours are separated by 0.01 eV; the position of the tube walls is indicated by the solid grey areas. The scenarios involve C_{60} encapsulation through (a) the open end of an isolated $(10, 10)$ nanotube, (b) the open end of bundled $(10, 10)$ nanotubes, and (c) a large opening in the $(10, 10)$ nanotube wall, centred in the $x-y$ plane. From [111], © American Physical Society.

edges of a large defect in the tube wall, representing an extended vacancy formed during the harsh purification process[7].

When following an 'optimum' trajectory starting outside the tube, a C_{60} molecule may first physisorb on the outer wall, thus gaining ≈ 0.07 eV. Our energy contour plots in figure 7 suggest

---

[7] We consider a defect formed by removing 76 atoms from the wall, with a diameter of ≈ 13.6 Å, just large enough to permit the unhindered entry of a C_{60} molecule.
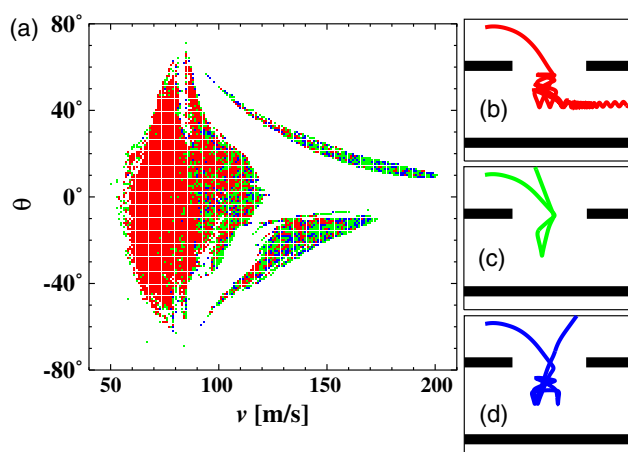
Figure 8. (a) Scatter diagram showing the probable outcome of C_{60} encapsulation through a large opening in the wall of a (10, 10) nanotube, as a function of the fullerene launch velocity v and launch angle θ. Events are colour coded according to the final state. Conditions that do not lead to encapsulation are marked in white. Conditions leading to encapsulation, with a sample trajectory shown in (b), are marked in red. Initial conditions and corresponding trajectories involving a temporary entry of the fullerene into the tube, followed by an escape after multiple scattering events, are shown in green if the final velocity has a negative x-component (c) and in blue if the final velocity has a positive x-component (d). From [111], © American Physical Society.

that the fullerene diffuses virtually freely along the tube wall. Since the adsorption potential is relatively shallow, the fullerene's angular velocity along the perimeter is limited by requiring the centrifugal force not to exceed a critical value for radial detachment. Consequently, the fullerene should follow a near-axial helical trajectory within a narrow 1D channel in the $x-y$ plane during its diffusive motion along the tube surface. Due to the large inertia of the C_{60} molecule and the absence of corrugations along the potential energy surface, virtually no rotations are excited as the fullerene slides along the tube wall. Upon entering the nanotube, the C_{60} gains an additional 0.36 eV [113].

The absence of activation barriers for all fullerene encapsulation scenarios depicted in figure 7 is surprising for two reasons. First, it suggests that the strong attraction to the under-coordinated atoms at the tube or defect edges does not trap the fullerene, but only modifies the entry channel without hindering the encapsulation (see footnote 6). Second, it leaves the origin of the observed optimum temperature of ≈400 °C for C_{60} encapsulation an open question.

The likelihood of C_{60} encapsulation depends on its initial conditions and the topology of the entire potential energy surface, as suggested by the sample trajectories in figure 7. In our molecular dynamics simulations, we initially placed the C_{60} molecule at equilibrium radial distance from the tube. We then calculated C_{60} trajectories in the $x-y$ plane using time steps of 5×10^{-16} s, by varying the launch speed v from 0–300 m s^{-1} in 1 m s^{-1} increments and the launch angle θ with respect to the tube axis from $-90°$ to $+90°$ in 1° increments. The calculation of all 54 000 trajectories for each encapsulation pathway would not be computationally feasible without approximations. We described the fullerene–nanotube interaction by the potential energy surfaces presented in figure 7, thus implying that both the C_{60} and the nanotube are structurally rigid.

For each set of initial conditions, we found that the ultimate outcome of each trajectory regarding encapsulation is decided within less than 10^6 time steps. We also found that all physically interesting phenomena occur within a velocity range between 50 and 200 m s^{-1},

the lower bound marking the onset of C_{60} mobility along the tube. The upper end of this range corresponds to high temperatures, at which fragmentation and tube fusion are to be expected. Consequently, we will discuss the encapsulation under the specific scenarios within this velocity range.

We found the encapsulation process through the end of an isolated nanotube, depicted in figure 7(a), to be very ineffective, the main reason being the relatively narrow and shallow channel in the potential energy surface of figure 7(a), which the fullerene must follow to reach the inside of the tube. Somewhat surprisingly, we did not find the probability of encapsulation to increase at the end of a nanotube bundle, consisting of (10, 10) tubes with an inter-wall separation of 3.4 Å, depicted in figure 7(b). We conclude that even in the case of a bundle, mainly due to the narrow entry channel at the end of the nanotubes, the probability of encapsulation through the end is rather low.

The outcome of the encapsulation process through a large opening in the side wall of the (10, 10) nanotube, depicted in figure 7(c), is shown as a scatter diagram in figure 8(a). In comparison to encapsulation through the open end of isolated or bundled nanotubes, the scatter diagram of figure 8(a) suggests a 30-fold increase of the cross-section for the C_{60} entry. In the following, we focus on the encapsulation through the large wall opening as the most likely process leading to peapod formation.

The scatter diagram of figure 8(a) shows a complex pattern consisting of large areas corresponding to the C_{60} entering the tube. Among these events, we have marked those trajectories leading to a definitive encapsulation, as depicted in figure 8(b), in red. The 'green' and 'blue' trajectories, shown in figures 8(c) and (d), involve a temporary entry of the C_{60} molecule into the tube. In that case, after multiple scattering events the fullerene may eventually escape in the backward ('green event') or the forward direction ('blue event'). Since such multiple scattering processes are chaotic, the 'blue' and 'green' events are homogeneously intermixed rather than separated into specific regions in figure 8(a).

To interpret the complex pattern in the scatter diagram of figure 8(a), we took a closer look at the individual trajectories. For launch velocities below 50 m s^{-1}, the C_{60} becomes trapped in one of the local minima and never reaches the defect. The highest probability of a successful encapsulation with an axial launch ($\theta = 0°$) is achieved at velocities in the range 50 m s$^{-1} \lesssim v \lesssim 120$ m s^{-1}. Axial launches with velocities exceeding $\approx$120 m s^{-1} overshoot the hole. C_{60} encapsulation is still possible for fast launches, but requires large launch angles and involves one or several radial reflections off the wall, as shown schematically in figure 7(c). For a given non-zero launch angle, the largest launch velocity allowing the fullerene to enter the tube involves a straight trajectory with no radial reflections. This is the case for the trajectories depicted in figures 8(b)–(d), for launch angles $\theta \approx 10°$ and $v \lesssim 200$ m s^{-1}. At lower launch velocities, a radial reflection from the tube wall causes the fullerene to overshoot the hole. As the velocity is reduced further, the point of first radial reflection is shifted closer to the launch site, allowing the fullerene to successfully enter the nanotube again. At a constant launch angle such as $\theta = 40°$, we can distinguish up to seven alternating regions associated with 'successful' and 'unsuccessful' trajectories. Each of these contiguous regions in figure 8(a) can be characterized by the number of radial reflections between the launch site and the hole edge.

Probably the most important result is that, in the absence of inelastic scattering, the probability of successful encapsulation ('red' events) is largest in the velocity range 80–120 m s^{-1} and almost independent of the launch angle θ. This suggests that it is not the launch direction, but rather the kinetic energy of the C_{60} molecule that decides the outcome. In view of the restricted motion of the C_{60} molecule along the tube surface, which reduces the number of degrees of freedom, we find that this velocity window translates into a kinetic temperature of the C_{60} close to 400 °C.

It is remarkable that the optimum temperature for peapod formation, as predicted by our calculation, falls into the observed temperature range 350–450 °C [102]. Previous explanations of this optimum temperature window were only based on plausibility arguments suggesting a low C_{60} mobility at low temperatures and a closure of the wall defects or fullerene fusion [114] under annealing conditions. We believe that the quantitative agreement between theory and observation also provides indirect evidence that the microscopic encapsulation mechanism involves defects in the tube wall.

Our calculations discussed so far have been based on the assumption that the microscopic degrees of freedom are decoupled from the macroscopic motion of the C_{60} molecule. Effectively, the possibility of energy transfer between the macroscopic and microscopic degrees of freedom introduces a damping mechanism. This new inelastic channel could convert some of the 'green' and 'blue' trajectories, depicted in figure 8, into successful encapsulation events, thus further increasing the cross-section for C_{60} encapsulation.

3.5.2. Nanotube peapods as nanoscale memory.   One of the possible application of nanotube peapods, described above, is in data storage. As a nanometre-sized counterpart of the oriental abacus, peapods viewed as a 'bucky-shuttle' [115] could combine high switching speed, high packing density and stability with non-volatility of the stored data [104].

The system described in the following, containing one fullerene in a nanotube capsule, was synthesized by thermally annealing nanodiamond powder, yielding structures such as that shown in figure 9(a). Figure 9(b) illustrates a corresponding model, consisting of a C_{60} encapsulated in a C_{480} capsule. The energetics of the $C_{60}@C_{480}$ system is shown in figure 9(c). The ends of the outer capsule are halves of the C_{240} fullerene, the optimum structures to hold a C_{60} molecule at an inter-wall distance of 3.4 Å. These end-caps connect seamlessly to the cylindrical portion of the capsule, a 1.5 nm long segment of the (10, 10) nanotube [47].

The interaction between the unmodified C_{60} molecule and the enclosing capsule is similar to that found in C_{60} crystals and nanotube bundles [47]; it is dominated by a van der Waals and a weak covalent inter-wall interaction that is proportional to the contact area between the constituents. An additional image charge interaction, which is nearly independent of the C_{60} position, occurs if the C_{60} molecule carries a net positive charge, as we discuss below. Obviously, the van der Waals interaction stabilizes the C_{60} molecule at either end of the capsule, where the contact area is largest. This is reflected in the potential energy behaviour in figure 9(c), and results in the likelihood of C_{60} to be found near the ends of the capsule, as evidenced in figure 9(a). In the following, we will study the possibility of information storage in this two-level system.

The usefulness of this nanostructure for data storage implies the possibility of *writing and reading* information quickly and reliably. Of equal importance is the capability to *address* the stored data efficiently, and the *non-volatility* of the stored information.

In order to move the encapsulated C_{60} from one end of the capsule to the other (the molecular analogue of writing) and to determine its position within the capsule (the molecular analogue of reading) most efficiently, the C_{60} should carry a net charge. In the $K@C_{60}$ complex, which is known to form spontaneously under synthesis conditions in the presence of potassium, the valence electron of the encapsulated K atom is completely transferred to the C_{60} shell [116]. The C_{60} is likely to transfer the extra electron to the graphitic outer capsule, since the ionization potential of $K@C_{60}$ is smaller than the work function of graphite. The extra electron will likely be further transferred to the (graphitic) structure that holds this element in place. Since the enclosed K^{+} ion does not modify the chemical nature of C_{60}, we will model the dynamics of the $K@C_{60}^{+}$ ion in the neutral C_{480} capsule by uniformly distributing a static charge of +1 e over the C_{60} shell.
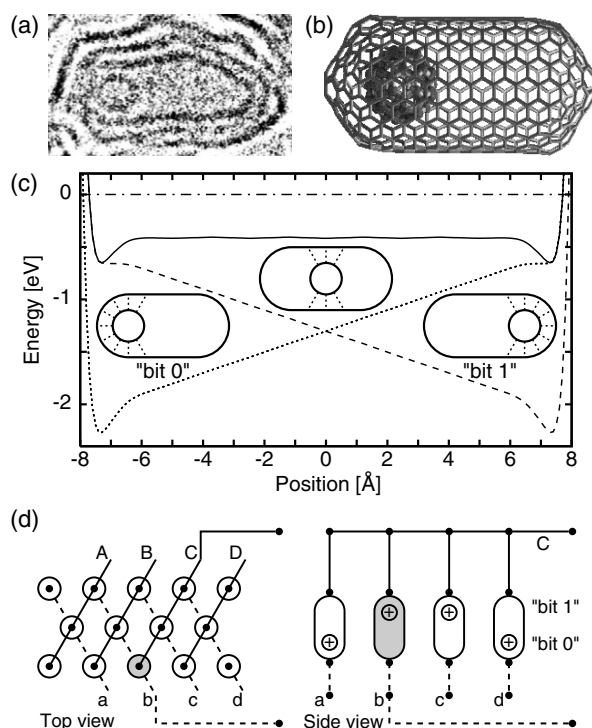
Figure 9. (a) Transmission electron microscope image of a 'bucky-shuttle', formed by annealing nanodiamond powder. (b) Structural model for an isolated K@C$_{60}^+$@C$_{480}$ bucky-shuttle, with the K@C$_{60}^+$ ion in the 'bit 0' position. (c) Potential energy of K@C$_{60}^+$ as a function of its position with respect to the outer capsule in zero field (solid curve) and switching field $E_s = 0.1$ V Å^{-1} (dashed curves). The K@C$_{60}^+$ ion position, representing the information, can be changed by applying this switching field between the ends of the capsule. Energy zero corresponds to an isolated K@C$_{60}^+$ at infinite separation from the C$_{480}$ capsule. (d) Schematic of a high-density memory board in top and side view. When a switching voltage is applied between conductors b and C, the corresponding bit information will be stored in the memory element bC at their intersection, shown shaded. From [104], © American Physical Society.

The *writing process* corresponds to switching the equilibrium position of the C$_{60}^+$ ion between the 'bit 0' and the 'bit 1' ends of the capsule in an applied electric field. This is best achieved if the connecting electrodes, supplying the bias voltage, are integral parts of the end caps, to reduce the field screening by the nanotube [117]. The energetics of C$_{60}^+$ in the switching field $E_s = \pm 0.1$ V Å^{-1}, generated by applying a voltage of ≈ 1.5 V between the end caps, is displayed in figure 9(c). One of the local minima becomes unstable above a critical field strength, causing the C$_{60}^+$ ion to move to the only stable position. The switching field $E_s = 0.1$ V Å^{-1} is small and will have no effect on the integrity of the carbon bucky-shuttle, since graphitic structures disintegrate only in fields $E \gtrsim 3$ V Å^{-1} [118, 119].

The information, physically stored in the position of the C$_{60}^+$ ion within the capsule, can be *read non-destructively* by detecting the polarity of the capsule. An alternative *destructive read* process would involve measuring the current pulse in the connecting wires, caused by the motion of the C$_{60}^+$ ion due to an applied probing voltage. The total charge transfer associated with the current pulse, which is one electron in our case, may be increased by connecting several capsules in parallel to represent one bit, and by using higher charged complexes such as La@C$_{82}^{2+}$.

When targeting high storage densities, the *addressability* of the stored information becomes important. One possible way to realize a high-density memory board is presented in figure 9(d). Maximum density is achieved by packing the nanotube memory elements like eggs in a carton. Rows of nanocapsules can be connected at the top and at the bottom by nanowire electrodes in such a way that a single memory element is addressed at their crossing point. Applying a switching voltage between two crossing electrodes (e.g. the bC pair in figure 9(d)) will generate a non-zero field only in the memory element labeled bC. As in the ferrite matrix memory, many memory elements can be addressed in parallel using such an addressing scheme. This arrangement applies both for the writing and the destructive reading processes described above, and allows for multiple bits to be written and read in parallel. In the latter case, the status of the memory element bC is inspected by applying a switching voltage between the electrode pair b, C, and monitoring the current in these electrodes.

Unlike in presently used dynamic random access memory (DRAM) elements, where information has to be sustained by an external power source, the *non-volatility of the stored information* results from a non-zero trap potential near the 'bit 0' or 'bit 1' end of the capsule. Thermal stability and non-volatility of data depend on the depth of this trap potential, which in turn can be adjusted by changing the encapsulated fullerene complex. The calculated trap potential depth of ≈ 0.24 eV for the $K@C_{60}^{+}$ ion near the ends of the capsule in zero field suggests that stored information should be stable well beyond room temperature and require temperatures $T \gtrsim 3000$ K to be destroyed. Further improvement of the thermal stability could be achieved using higher-charged endohedral complexes containing di- or trivalent donor atoms, such as $La@C_{82}$ discussed above.

To study the efficiency of the writing process, we performed a molecular dynamics simulation of the switching process from 'bit 0' to 'bit 1' in the microcanonical ensemble of the $C_{60}^{+}@C_{480}$ memory element. We used the total energy functional of equation (2) [12], augmented by long-range van der Waals interactions [120]. Our computationally efficient $O(N)$ approach to determine the forces on individual atoms [13] had been previously used with success to describe the disintegration dynamics of fullerenes [121] and the growth of multi-wall nanotubes [122]. A time step of 5×10^{-16} s and a fifth-order Runge–Kutta interpolation scheme was used to guarantee a total energy conservation of $\Delta E/E \lesssim 10^{-10}$ between successive time steps.

The results of our simulation are shown in figure 10. Initially, the C_{60}^{+} ion is equilibrated near the 'bit 0' position. At time $t = 0$, a constant electric field of 0.1 V $Å^{-1}$ is applied along the axis of the outer capsule. The originally stable 'bit 0' configuration becomes unstable in the modified total energy surface, depicted in figure 9(c). The C_{60}^{+} ion is subject to a constant acceleration to the right, and reaches the 'bit 1' position only 4 ps later, as seen in figure 10(a). During this switching process, the potential energy lost by the C_{60}^{+} ion is converted into kinetic energy, as seen in figure 10(b). Due to the small (albeit non-negligible) interaction between the encapsulated ion and the capsule, the kinetic energy gained initially occurs as rigid-body translational energy of the C_{60}^{+} ion. A nearly negligible energy transfer into the internal degrees of freedom due to atomic-scale friction, manifested in a very small increase of the vibrational temperature in figure 10(c), is observed during this initial stage of the switching process.

4 ps after the switching field is applied, the C_{60}^{+} ion reaches the opposite end of the capsule, having gained 1.5 eV of net kinetic energy. This kinetic energy is too small to damage the capsule, as inelastic collisions involving C_{60} require energies exceeding 200 eV to occur [123]. Upon impact onto the enclosing capsule from the inside, a substantial fraction of this energy is converted into heat, thus increasing the vibrational temperature of the outer capsule by $\lesssim 10$ K and that of the C_{60}^{+} ion by ≈ 2 K. Due to the high heat conductivity and melting temperature
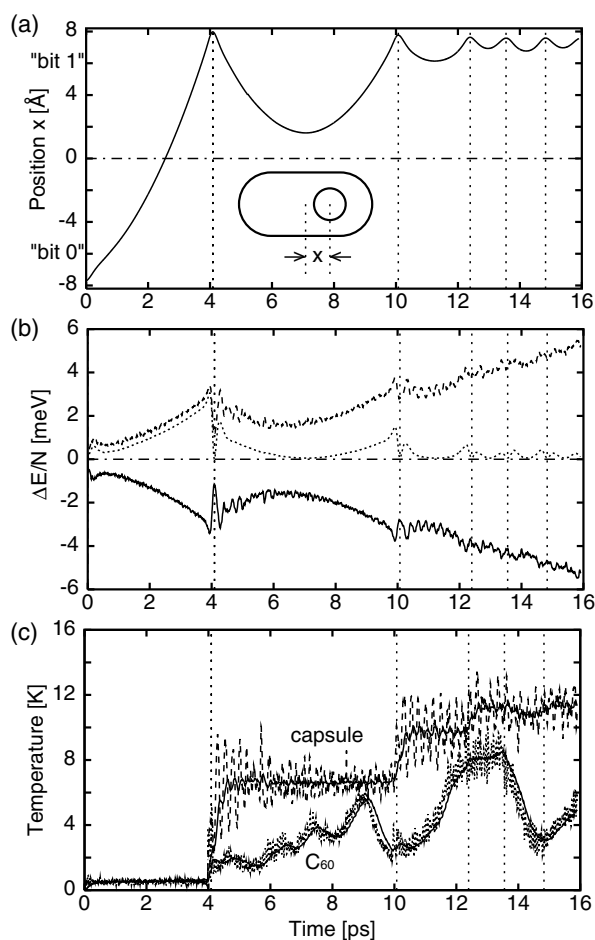
Figure 10. Results of a molecular dynamics simulation of the switching process from 'bit 0' to 'bit 1', when a constant electric field of 0.1 V $Å^{-1}$ is applied along the axis of the capsule. (a) Position of the $K@C_{60}^{+}$ ion with respect to the centre of the enclosing C_{480} capsule as a function of time. (b) Changes in the potential energy (solid curve) and kinetic energy (dashed curve) in the laboratory reference frame as a function of time. The portion of the kinetic energy, corresponding to the translation of the enclosed $K@C_{60}^{+}$ ion with respect to the capsule (dotted line), is seen to decrease as the system temperature rises. The total energy (dash–dotted line) is conserved. All energies are given per atom. (c) Vibrational temperature of the enclosed $K@C_{60}^{+}$ ion (dotted line) and the enclosing capsule (dashed curve) as a function of time. The solid curves are backward convolutions of the vibrational temperature values, using a Gaussian with a full-width at half maximum of 7.5×10^{-13} s. From [104], © American Physical Society.

$T_{\mathrm{M}} \lesssim 4000$ K of graphitic nanostructures [121], this modest heat evolution is unlikely to cause any structural damage even at high access rates.

As seen in figure 10(b), the net kinetic energy of the encapsulated C_{60}^{+} with respect to the outer capsule is significantly reduced during this collision. The C_{60}^{+} bounces back towards the middle of the capsule, slowed down by the opposing electric field, and finally turns again towards the 'bit 1' end. Figure 10(c) indicates that thermal equilibration in the system after the collision is achieved stepwise. The step period of ≈ 1 ps results from the beats between the low-frequency quadrupolar deformation modes of the colder encapsulated C_{60}^{+} ion and the hotter enclosing capsule, which have been excited during the quasielastic collision.

One or few oscillations of the C_{60}^+ ion inside the enclosing capsule, damped by transferring energy from macroscopic to internal degrees of freedom, are necessary to stabilize it in the new equilibrium 'bit 1' position, with a kinetic energy not exceeding the depth of the trap potential. As seen in figure 10(b), this situation occurs ≈ 10 ps after the initial onset of the switching field, thus resulting in an ideal memory switching and access rate close to 0.1 THz. In the slower sequential mode, this translates into a data throughput rate of 10 GB s^{-1}, four orders of magnitude faster than the data throughput rate of 4–5 MB s^{-1} which is achieved presently in magnetic mass storage devices.

4. Structural transformations in fullerenes and nanotubes

Due to the unusual stability of the graphitic sp^2 bond, large-scale structural changes in bulk fullerene crystals and related systems occur only under extremely high pressures and temperatures [124–129]. On the other hand, fullerenes in nanotube peapods [99] have been observed to fuse [102, 114] at relatively low temperatures near 1100 °C, significantly below the decomposition temperature of fullerenes [121] or graphite [130] near 4000 °C. Similarly puzzling is the observation of rapid nanotube fusion at relatively low temperatures, implying a process with a very low activation barrier [114, 131]. In view of the fact that even minor structural changes in carbon nanostructures may modify significantly their physical properties, including magnetism [58, 132], there is additional interest in understanding fusion as a way of controlling large-scale structural transformations. A detailed understanding of such large-scale structural rearrangements in sp^2 bonded systems may open a route to directing the assembly of even more complex functional nanostructures.

4.1. Fusion of fullerenes in peapods

The following computational study elucidates the microscopic fusion mechanism of fullerenes. We show that large-scale structural changes, including fusion, can be achieved by a finite sequence of generalized Stone–Wales transformations, which involve only bond rotations and avoid bond breaking. The optimum sequence of bond rotations, which leads to fusion, may be determined using a graphical search program [133]. Detailed information about the atomic trajectories associated with the minimum energy pathway can further be obtained from a phase space search using the 'string method'. These studies provide also valuable information regarding the activation barriers and transition-state geometries.

We calculate the total energy of the fullerene system using the total energy functional of equation (2) [12]. The numerical results are compared to those of *ab initio* density functional calculations, which use a numerical basis to represent localized atomic orbitals [74], and which have been applied successfully to nanotubes and fullerenes [75]. Structural optimization is performed using the conjugate gradient technique. Our total energy formalism describes accurately not only the covalent bonding within the sp^2 bonded fullerenes, but also the weak interaction between fullerenes. We find it crucial to use an electronic Hamiltonian in this study, since analytical bond-order potentials do not describe the rehybridization during the fusion process with sufficient precision.

The fusion of two C_{60} molecules to a C_{120} capsule, which has been observed in peapods [102, 114], is driven by the energy gain associated with reducing the local curvature in the system. Still, this reaction involves a large-scale morphological change and will only occur if the required activation barrier is small.

A previous study [134], based on minimizing the classical action, suggests that the fusion reaction should be a multi-step process. Due to the computational limitations associated
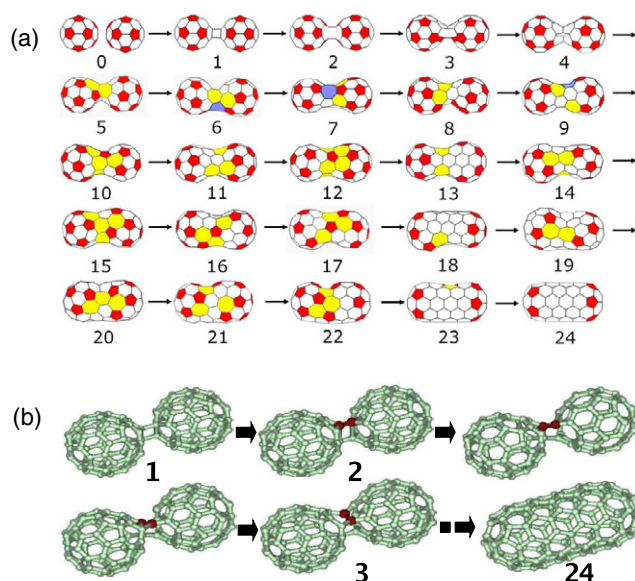
Figure 11. Microscopic mechanism of fullerene fusion in peapods. (a) Optimum pathway for the $2C_{60} \rightarrow C_{120}$ fusion reaction, involving the smallest number of generalized Stone–Wales bond rotations, determined by a graphical search of all possible bond rotation sequences [139]. Polygons other than hexagons are emphasized by colour and shading. (b) Snapshots of the optimized initial and final structures, and the metastable structures '2' and '3', depicted in (a). Also shown are two intermediate structures along the optimum fusion pathway between '2' and '3', resulting from the phase space search by the 'string method'. The bond involved in the $2 \rightarrow 3$ Stone–Wales transformation is emphasized by dark colour. From [108], © American Physical Society.

with the formidable task to find a contiguous minimum-energy path in the 360-dimensional configurational space of the system, and to anticipate the optimum one-to-one atomic mapping between the initial and the final structure, we expect the 'true' activation barrier for this reaction to lie below the relatively high postulated value of ≈ 8 eV. Combining a very similar total energy functional with a method to identify all intermediate steps, we identify in the following an alternate reaction path with lower activation barriers.

It appears that the most likely fusion path may involve a sequence of bond rotations, called generalized Stone–Wales (GSW) transformations. GSW transformations are known to require much lower activation energies than processes involving bond breaking, and have been studied extensively in sp^2 bonded carbon structures [133, 135, 136]. A possible GSW pathway for fusion has been suggested based on a 'qualitative reasoning assisted search' for structures along the minimum-energy path [137, 138]. The initial step in that study, however, is a reaction between two pentagons facing each other, which is energetically unaccessible.

In order to obtain microscopic insight into the fusion reaction, avoiding the above shortcomings, we investigated the optimum reaction path for the $2C_{60} \rightarrow C_{120}$ fusion. It is well established that polymerization [140] and subsequent fusion [139, 141–143] of fullerenes starts by the (2 + 2) cycloaddition reaction. This reaction, depicted as the $0 \rightarrow 1$ transition in figure 11(a), requires two 'double bonds', which connect adjacent hexagons in the C_{60} molecule, to face each other at the contact point of adjacent fullerenes.

With the (2 + 2) cycloaddition reaction completed, we investigated the possibility to complete the $2C_{60} \rightarrow C_{120}$ fusion by generalized Stone–Wales transformations only. We searched all topologically possible pathways for the reaction with the aid of a graphical
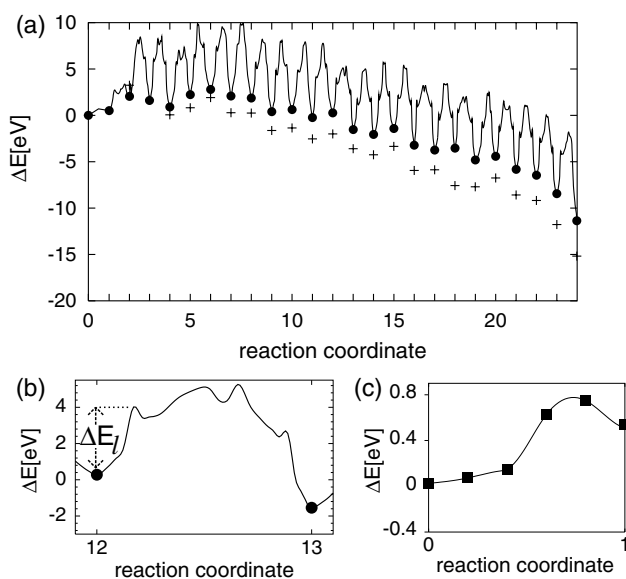
Figure 12. Energetics of the fullerene fusion in peapods. (a) Energy change along the optimum reaction path, given by the solid line[8]. Energy results for the 25 intermediate structures, shown in figure 11, based on our total energy functional ($\bullet$), are compared to *ab initio* density functional results ($+$). The contiguous minimum energy path in configurational space was identified using a 'string' technique. (b) Details of the energy change along the optimum path between structures '12' and '13' of figure 11, showing several local minima and implying a multi-step nature of this Stone–Wales transformation. The activation barrier limiting the reaction rate is denoted by ΔE_l. (c) Energetics of the $(2+2)$ cycloaddition reaction, corresponding to the $0 \rightarrow 1$ transition in figure 11(a), which is a necessary prerequisite for the fusion process. From [108], © American Physical Society.

search program [133, 139]. Among these, we identified the shortest pathway, which is likely associated with the fastest fusion mechanism. This pathway involves only 23 GSW transformations and is depicted in figure 11(a). Tracing the atomic positions during this structural rearrangement, we found that the diffusion range of individual carbon atoms is limited to about three atomic bond lengths in the structure. Snapshots of intermediate state geometries along the optimum fusion pathway are shown in figure 11(b).

The energetics of the $2C_{60} \rightarrow C_{120}$ fusion process along the optimum path is depicted in figure 12(a). The energy results for the optimized metastable states of figure 11(a) are given by the data points. We conclude that the *ab initio* density functional and our parametrized total energy functional give consistent results for the relative energies of the intermediate states[9], and also for the large net energy gain of ≈ 13 eV associated with the fusion.

We employed the recently developed 'string' method [144, 145] to efficiently determine the detailed minimum energy path, including identifying the reaction barriers of individual GSW transformations between the 24 intermediate states. This method represents the reaction pathway connecting the initial and final 120-atom geometry in the 360-dimensional atomic

---

[8] For an intuitive interpretation, the distance between adjacent points along the reaction cordinate represents the maximum atomic displacement in the structure.

[9] For the sake of comparison, we also calculated the activation barrier for a GSW transformation in a graphene sheet and obtained a much larger value of ≈ 9 eV, which compares well with the published value of ≈ 8 eV based on *ab initio* calculations [146].

configuration space by a string line. The string is initially subdivided into finite segments of equal length, connecting structural replicas. For an optimum path, we require that the atomic force acting on each replica has a vanishing component normal to the string. We employ 60–100 replicas for each GSW step and relax the atomic positions, until the normal component of the atomic force becomes less than 0.05 eV Å^{-1} in magnitude.

Close inspection of the reaction energy along the contiguous optimum fusion path in figure 12(a) indicates a sequence of 23 activated processes connecting the 24 metastable states. We find the activation energy barriers $\Delta E_{\text{GSW}} \approx 5$ eV of these GSW transformations to be significantly lower than in graphite [146], as expected for Stone–Wales processes in non-planar structures due to the deviation from sp^2-bonding. In the presence of extra carbon atoms, the activation barriers for GSW transformations may be lowered further to below 4 eV by autocatalytic reactions [147, 148]. Also, under electron irradiation, this process can proceed relatively quickly in view of the high rate of sub-threshold energy transfer to the structure [149]. In extended fullerene systems, moreover, the energy release during the fusion process should heat up the structure locally, thus further promoting activated processes in the local vicinity.

Maybe the most significant finding of our study is the occurrence of multiple shallow local energy minima in the course of each GSW transformation. Details for the energy landscape, associated with the $12 \rightarrow 13$ reaction, are shown in figure 12(b). This implies that GSW transformations are multi-step rather than single-step [150] or two-step [151–153] processes, as postulated earlier. The local minima originate from global stress release during the bond rotation, which can be viewed as breaking two C–C bonds at the same time as new bonds are being formed. Performing unconstrained conjugate gradient structure optimization at the local extrema, we confirmed the presence of local energy minima and were able to identify the geometry of the transition states in-between. We notice that GSW transformations are multi-step processes only in non-planar structures, as no such local minima occur during Stone–Wales transformations in a graphene layer due to the absence of tensile stress in that system.

To estimate the overall reaction time at the temperature of $1100\,^{\circ}$C, where the onset of fusion has been observed [102, 114], we considered the fusion process as a sequence of 23 GSW transformations. Assuming the attempt frequency of 3×10^{13} Hz for the GSW transfomations [148] and a limiting activation barrier $\Delta E_l = 4.5$ eV in the Arrhenius formula[10], we find that the fusion reaction should be completed in 7 hours. Reduction of the activation barrier by 0.5 eV should reduce the total fusion time to 6 minutes. In view of the fact that fusion is generally more complex than an optimum sequence of GSW transformations, these values agree well with the observed fusion time of several hours [102, 114].

In spite of its relatively low activation barrier depicted in figure 12(c), the initial $(2 + 2)$ cycloaddition reaction between the structures '0' and '1' may play an important, possibly even the rate-limiting, role in the fusion process. Fusion can only be initiated in the optimum geometry, where two double bonds in adjacent fullerenes face each other at the contact point. The probability of this configuration appears as a factor in the attempt frequency ν of the $0 \rightarrow 1$ reaction in the Arrhenius formula (see footnote 10) and thus reduces the reaction rate, since the low activation barrier of ≈ 0.7 eV only applies to attempts with the optimum fullerene orientation.

At low temperatures, polygons rather than double bonds should preferentially face each other in adjacent fullerenes, effectively preventing the fusion. Only at high enough temperatures, when unhindered fullerene rotation is activated [154], will the probability of double bonds facing each other increase, while each fullerene probes the configurational space.

---

[10] The Arrhenius formula determines the reaction rate as $\nu \exp(-\Delta E / k_{\text{B}} T)$, where ν is the attempt frequency, ΔE the activation barrier, k_{B} the Boltzmann constant, and T the temperature.

At that moment, the (2 + 2) cycloaddition reaction should stop the rotation [155], and may initiate fusion.

To estimate the probability of the configuration required for the (2 + 2) cycloaddition to occur, we first consider the phase space describing the motion of two rigid fullerenes at constant equilibrium distance (structure '0' in figure 11), which are freely rotating in space. The eight-dimensional configurational space, spanned by the three Euler angles defining the orientation of each fullerene and the two-dimensional vector defining the orientation of the inter-fullerene connection, is explored uniformly by the rotating fullerenes. Next, we assume that the difference between a 'correct' and an 'incorrect' fullerene alignment corresponds to a misorientation exceeding $\Delta\varphi \gtrsim 1°$ in any dimension, which naturally introduces a grain size for the discretized configurational space.

In view of the fact that each fullerene has thirty double bonds, each of which can have two orientations, 3600 out of 3×10^{19} cells in this space represent favourable configurations. Assuming that the configurational space exploration by the freely rotating fullerenes occurs at random in-between two cycloaddition attempts, separated by the period of the inter-fullerene vibration, the probability of finding an optimum configuration is $\approx 10^{-14}$. Using $\nu = 7 \times 10^{12}$ Hz for the inter-fullerene vibration frequency [156], the (2 + 2) cycloaddition step with an activation barrier $\Delta E = 0.725$ eV should occur on the timescale of one week at $1100\,°C$, significantly longer than the timeframe of a GSW transformation. Thus, this step should be rate limiting in a close-packed three-dimensional C_{60} system, which, while molten at this temperature, could be prevented from evaporation by external pressure.

Restricting the configurational space to one dimension, which occurs when chains of fullerenes are packed in peapods, increases the fusion probability substantially. The crucial role played by the enclosing nanotube is to keep adjacent fullerenes in place long enough for them to probe the configurational space at close range. Since the vector connecting adjacent fullerenes coincides with the nanotube axis, the possibility of non-central collisions is eliminated, the dimensionality of the configurational space is reduced to six, and the number of discrete cells to only 5×10^{14}. This increases the probability of the optimum fullerene orientation by five orders of magnitude, and reduces the reaction time of the (2 + 2) cycloaddition step to only 7 seconds at $1100\,°C$. We conclude that fusion should occur more easily when fullerenes are packed in peapods than in three-dimensional bulk C_{60}.

In a three-dimensional C_{60} system, the fusion rate should further be reduced due to the fact that more than one GSW transformation involving the same fullerene may occur simultaneously. Each C_{60} molecule has initially the ability to form at least four initial connections with neighbouring fullerenes by the (2 + 2) cycloaddition reaction [126–129]. Considering the finite size of the C_{60} molecule, GSW transformations associated with one fusion reaction are likely to interfere with the transformation necessary for a separate fusion reaction occurring concurrently. Due to resulting frustration, the activation barriers of individual GSW transformations could increase significantly, possibly even stopping the fusion. Since this effect is less severe in lower dimensions, the reduction of the overall fusion rate associated with concurring binary fusion reactions should be much less important in one-dimensional peapods than in bulk C_{60}.

4.2. Fusion of nanotubes

Similar reasoning as applied to fusing fullerenes may be beneficial to elucidate the efficient fusion of adjacent nanotubes [114, 131, 145] depicted in figure 13. Fusion pathways that have been discussed so far involve vacancy generation to establish a local connection between tubes and to propagate this connection as the tubes merge [131]. Yet the high energy cost associated
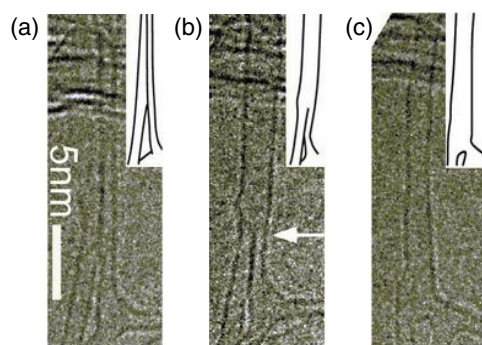
Figure 13. Time sequence of high resolution transmission electron microscope images evidencing the zipper process for the coalescence of two SWNTs. (a) Tubes prior to coalescence at 800 °C. (b) As electron irradiation continues, the nanotubes get closer, overlap and start merging into one. The fused region is emphasized by the white arrow. (c) The coalescence process is completed as the fusion region moves down, completing the zipper closure. From [145], © American Physical Society.

with bond breaking is inconsistent with the high speed of the fusion process following the formation of the initial connection. In analogy to the fusion of fullerenes discussed above [108], a microscopic zipper mechanism that involves bond rotations only offers a viable explanation for the efficient fusion of adjacent nanotubes [145].

The Y-junction structure used in our study of nanotube fusion, resembling the shape of trousers, is shown in figure 14(a). This generic structure forms when, in presence of atomic defects, a local connection is established between adjacent nanotubes. The structure consists of a $(10, 10)$ nanotube section representing the waist and two $(5, 5)$ nanotubes representing the legs, and could be created by bond rearrangement during electron irradiation under experimental conditions. The bonding topology in the defective region, where the tubes are connected, is vacancy-free, which has never been considered before. The junction region shows negative Gaussian curvature. It contains higher polygons, including heptagons or octagons, inserted in the sp^2-bonded hexagonal network forming the tubes. Here, we show that a continuous fusion process is possible in this geometry. In view of the instability associated with the insertion of higher polygons, we focused on Y-junction geometries containing only heptagons and octagons in the hexagon network.

Our main objective is to find out if it is possible to advance the axial position of the defect region and thus to merge the tubes by means of bond rotations only, similar to a zipper that reversibly connects or disconnects two pieces of fabric. In order to find all acceptable pathways leading to coalescence, a non-trivial topological problem, we use a graphical search program that was initially developed to study the fusion of fullerenes [139]. Since the initial steps of the local bridge formation between nanotubes and fullerenes are similar, we focus here on the major portion of the fusion process. Our search program generates all possible geometries, obtainable by a sequence of GSW bond rearrangements starting from one initial structure, and compares them to the target structure [139]. We restricted our search to GSW transformations [135, 157], which were initially proposed as a general mechanism for the inter-conversion between fullerene isomers [133, 158], discussed above. The main advantage of the GSW transformations is the low activation barrier, which accelerates the structural transformations in these vacancy-free systems during the zipper closure.

The zipper mechanism of nanotube fusion in the Y-junction geometry, containing one octagon and four heptagons in the junction region, is presented in figure 14. Figure 14(a) depicts
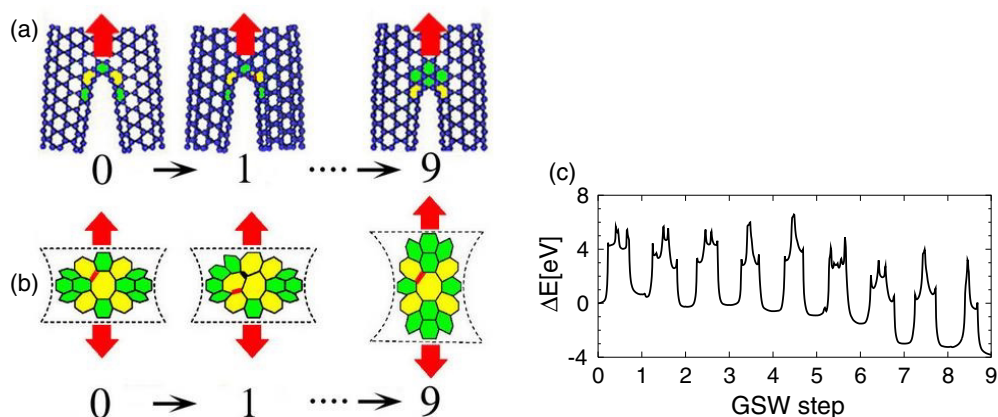
Figure 14. Zipper mechanism of the nanotube fusion in the Y-junction geometry of one of our model morphologies, containing one octagon and four heptagons in the junction area. Front view (a) and structural diagrams detailing the bond switching (b), as two (5, 5) nanotubes merge to a (10, 10) nanotube in a morphology reminiscent of 'trousers'. The fusion process requires nine GSW transformations to propagate the branching region axially by one period of the armchair nanotube without creating vacancies. Bonds, which are rotated during the individual GSW transformations, are emphasized by thick lines. Details of the complete process are presented at http://nanotube.msu.edu/ntyjct/. The calculated total energy change ΔE along the minimal energy path connecting the intermediate steps is shown in (c). From [145], © American Physical Society.

one transformation cycle in front view. The detailed bond rearrangements are displayed in figure 14(b) as structural diagrams. Each GSW step within the transformation cycle is identified by a rotation of a single bond near the junction of two (5, 5) nanotubes. We emphasize the respective bonds by a thick red line prior to, and a thick black line after, the rotation. Our results show that a sequence of only nine sequential GSW transformations is sufficient to propagate the connecting region by one step and thus increase the waist section axially by one period of the (10, 10) nanotube, at the expense of the leg section. Following such a full transformation cycle, the final structure ('9') is topologically equivalent to the initial structure ('0'). In an alternative geometry not discussed here, which contains six heptagons and no higher polygons in the junction region, the axial propagation of the junction by one period can be achieved by only twelve sequential GSW transformations. A related structural transformation, which involves an energetically unstable twelve-membered ring in the junction region, has also been found to provide a pathway to nanotube fusion [137, 138]. There, the GSW sequence has been determined using a 'qualitative reasoning assisted search' instead of a computer-assisted complete search. The energetics of the optimized fusion process discussed here, depicted in figure 14(c), suggest a monotonic stability increase upon each GSW transformation, in stark contrast to the findings of [137, 138].

As seen in figure 14(c), the fusion process is exothermic. Based on strain energies of infinite structures, we expect an energy gain of 4.8 eV by converting two 0.21 nm long (5, 5) nanotube segments to a (10, 10) nanotube within one transformation cycle [5]. Total energy calculations for the intermediate structures i, encountered during the fusion process and shown in figure 14(c), are performed using the total energy functional of equation (2) [12] for a 364-atom cluster representing the structure. All intermediate structures of the system have been fully relaxed using the conjugate gradient technique [159]. Our cluster calculation indicates that the energy is lowered by 4 eV during the complete 9-step transformation cycle, in good agreement with the above 4.8 eV value in view of the finite size of the cluster.

To evaluate the reaction barriers associated with each individual GSW transformation, which play a crucial role in the reaction rate of the zipping process and have not been investigated in [137, 138], we determine the minimum energy path in the configuration space using the 'string method' [144] discussed in section 4.1 in connection with the fusion of fullerenes.

The details of the reaction energy ΔE along the contiguous minimum-energy path, corresponding to the zipper process, are depicted in figure 14(c). These results suggest that most GSW transformations are multi-step processes with well-defined transition states, as discussed below. We find the maximum energy barrier for a single GSW step to lie near 5–6 eV. As we discuss in the following, this activated process can proceed relatively quickly under the experimental conditions in view of the high rate of sub-threshold energy transfer to the structure during electron irradiation [149]. Alternatively, the activation barrier for GSW transformations may be lowered to below 4 eV by autocatalysis reactions [147] involving extra carbon or nitrogen atoms [148]. The 5–6 eV activation energy for the GSW transformation in the Y-junction system lies significantly below the graphene sheet value of ≈9 eV based on our approach, or ≈8 eV based on *ab initio* calculations [146]. Such a lowering of the activation barrier is expected in non-planar structures due to the deviation from sp^2-bonding. We find this hypothesis confirmed in our calculations, since lower barriers are found when more heptagons or octagons are closer to the rotating bond.

As mentioned above, we find that most Stone–Wales transformations involve multiple shallow local energy minima, implying a multi-step process. These minima originate from local stress release, as two C–C bonds are being broken at the same time as other bonds are being formed during the bond rotation. The barriers surrounding these local minima are very small, suggesting a short lifetime with little effect on the overall reaction rate. In contrast to these findings in the nanotube Y-junction, no such local minima occur during the Stone–Wales transformation in graphite due to the absence of tensile stress in that system.

To investigate the effect of high temperatures on the activated fusion process and to identify a possible mechanism that would lower the activation barriers even further, we performed Nosé–Hoover molecular dynamics (MD) calculations at temperatures between 400 and 2400 K. The upper limit of this temperature range is determined by the onset of melting at 2800 K, which starts at the exposed edges of the finite Y-junction or 'trousers' structure. With increasing temperature, particular vibration modes are stepwise activated. Below 400 K, we observe only local atomic vibrations without global shape changes of the structure. At 800 K, a radial breathing mode of the tubes dominates the dynamics. At 1200 K, the 'legs' of the trousers structure exhibit a vibration mode, reminiscent of walking and twisting. At 1600 K, this 'walking' mode is replaced by a 'scissor' mode of the legs, which strains the junction region and lowers the activation barrier for GSW transformations [160–162].

5. Technological challenges

The continuing trend towards miniaturization, rapidly approaching the atomic scale [163], raises serious concerns about the required degree of perfection and defect tolerance of nanoscale devices. Carbon nanotubes [4], considered as functional building blocks [164] of such devices, can sustain very large current densities [164, 165] of 10^9 A cm^{-2}, and show an unusually high thermal and mechanical stability [19]. Nanotube-based transistors out-perform state-of-the-art silicon-based elements in terms of speed, on/off ratio, and the maximum current [165, 166].

However, substantial defect densities in currently available nanotubes raise a concern about the performance and reliability of nanotube-based devices. Theoretical studies showed that even individual vacancies change transport properties of these quasi one-dimensional systems

significantly [167, 168]. At particular bias voltages, drastic conductance reduction in nanotubes results from perturbing the π electron system, and from the presence of dangling bonds [168]. Another point of concern is whether defects may trigger failure earlier in nanoscale devices than in current Si-based devices. This concern is based on the fact that a 'ten-nine' purity requirement is currently being placed on silicon wafers in order to avoid device failure, which appears to be initiated by processes occurring at defect sites, in the electronically excited state [169, 170]. So far, little is known about possible microscopic processes that could lead to failure of defective nanotubes.

5.1. Defect tolerance of nanotubes subject to electronic excitations

In the following, we investigate the defect tolerance of nanotube components by monitoring the response of carbon nanotubes with atomic vacancies to electronic excitations [16]. Such excitations may be induced by interaction with electromagnetic radiation, or by electron–electron scattering in current-carrying nanotubes. Since nanostructures appear to be more susceptible to defects than bulk systems, we intuitively expect them to fail earlier. The major result of our theoretical study attests to the contrary. Rather than showing signs of premature failure, we find that nanotubes containing vacancies exhibit a unique self-healing mechanism, associated with the possibility of forming new bonds bridging the vacancy site. Such a self-healing process does not occur in submicron-scale Si-based devices, and is intimately linked to the nanometre size of our system.

Since atomic-scale processes leading to device failure in the electronic excited state occur on the sub-picosecond to picosecond timescale, they are very hard to track experimentally. As a viable alternative, which should provide microscopic information about atomic-scale processes occurring during failure, we propose the use of molecular dynamics (MD) simulations of defective carbon nanotubes subject to electronic excitations. This type of computational approach turns out to be particularly challenging, since the study precludes the solution of the time-dependent Schrödinger equation for the time evolution of the electronic wavefunctions in the presence of ionic motion, caused in turn by the changing charge distribution [11]. This computer intensive calculation has been performed using the recently developed first-principles simulation tool for electron–ion dynamics (FPSEID) [171, 172].

Since strained narrow nanotubes are suspected to be intrinsically most susceptible to failure, we focus in our study on the (3, 3) nanotube with a monatomic vacancy as a test case. Being only 0.4 nm in diameter, this is one of the narrowest nanotubes observed [173, 174]. To distinguish nanotube-specific intrinsic behaviour from effects caused by the nanotube environment in the experimental situation [174], we consider an isolated nanotube in vacuum. We use periodic boundary conditions throughout our simulations, also implying a periodic arrangement of vacancies with an axial separation of four to six primitive unit cell sizes of the defect-free nanotube. Consequently, the unit cells used in our calculation hold between 47 and 71 atoms.

We considered the relaxed monatomic vacancy structure in a (3, 3) carbon nanotube, depicted in the left panel of figure 15(a), as the starting point to investigate structural changes that may be induced by electronic excitations. The study was performed within the *ab initio* time-dependent density functional formalism coupled to molecular dynamics simulations (TDDFT-MD) [171, 172]. We applied the local density approximation to the density functional theory (DFT) [70, 71]. Valence electron states were described using Troullier–Martins type pseudopotentials [72] and a plane wave basis with the kinetic energy cutoff of 40 Ryd. Due to the large size of the unit cell representing the defective tube, we limited our sampling of the momentum space to the Γ point. Comparison with density functional calculations for

(a)

0 fs   100 fs   200 fs
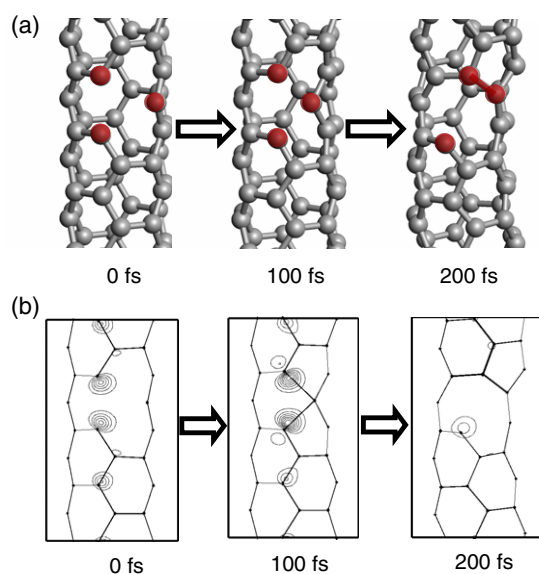
(b)

0 fs   100 fs   200 fs

Figure 15. Self-healing process within a (3, 3) nanotube with a monatomic vacancy, induced by illumination. (a) Time evolution of the geometry. The three atoms adjacent to the vacancy and the new C–C bond, which forms ≈200 fs after the electronic excitation, are emphasized by colour and shading. (b) Time evolution of the partial charge density associated with the excited electron state. The lowest contour lines are common to the three panels.

systems with a larger unit cell justifies the use of the Γ point approximation, which was also necessitated by the extremely high demand on computational resources.

In our excited-state dynamics simulation, we selected among the many possible excitations the particle–hole state localized at the vacancy site, which yields strong Hellmann–Feynman forces with a tendency to expand the vacancy site and thus to destroy the nanotube. We found this to be the case by promoting an electron from the highest occupied state to the second lowest unoccupied state. Following this optically allowed excitation, we noticed an energy reordering of the highest and second highest occupied states [175]. The energy of 0.9 eV associated with this excitation was determined from the total energy difference between the excited state and the ground state in a (3, 3) nanotube with a 47-atom unit cell. The subsequent time evolution of the electronic and atomic structure in this Franck–Condon like process was computed within the TDDFT-MD formalism, by maintaining self-consistency between the wavefunction and potential, which both evolve in time [171, 172]. We used extremely short time steps of 0.08 au, corresponding to 1.94×10^{-3} fs, to accurately describe the electron dynamics. This time step is three orders of magnitude shorter than used in ground state *ab initio* MD simulations, and necessitates very large computer resources to cover the typical timescale of subsequent atomic motion occurring over ≈10^2 fs.

At the beginning of the simulation, we froze all the atoms in the relaxed ground state geometry and obtained the static solution of the electronically excited state. The ion dynamics induced by this excitation is depicted as a time sequence of geometries in figure 15(a). We found that the vacancy initially started to open in the direction of the Hellmann–Feynman forces, suggesting a destructive tendency. 200 fs after the excitation, two of the three atoms adjacent to the vacancy approached each other sufficiently close to form a new bond. We interpret the formation of this new bond as a self-healing process, which is unique and extremely beneficial to this nanostructure.

The newly formed bond was found to bridge the initial gap by providing a new connection between atoms adjacent to the vacancy, thus restoring part of the initial structural rigidity and saturating some of the dangling bonds at the vacancy site. Since dangling bonds have been identified as important scattering centres [168], this reconstruction is expected to improve the conductance of the defective nanotube.

Our density functional calculations suggest that in the electronic excited state, the reconstruction occurs spontaneously, without additional thermal activation, on a timescale of 10^2 fs. This is very different from the ground state behaviour, where such a reconstruction is also possible, but requires an initial energy investment of 0.3 eV, followed by a net energy gain of about 1.76 eV/vacancy. Once the reconstruction is completed and the system returns to the ground state, the probability of reopening the monatomic vacancy at ambient temperatures is extremely small in view of the ≈2 eV activation barrier required for the reopening of the bond.

To understand the energy gain associated with this healing process in a broader context, we focused on the electronic ground state first, and performed structure optimization calculations of monatomic vacancies in various nanotubes. In narrow nanotubes, which are more flexible, the energy gain due to a new bond by far outweighs the strain related to the reconstruction, which can easily be accommodated locally. With 1.76 eV/vacancy, the net energy gain due to re-bonding is the largest in the (3, 3) nanotube. With increasing nanotube diameter, the strain extends over an increasing region, making this reconstruction energetically less favourable. This results in the net energy gain decreasing from 1.53 eV in the (5, 5) nanotube to 1.23 eV in the (7, 7) nanotube. In the even wider (10, 10) nanotube, the closure of the monatomic vacancy appears to be energetically unfavourable [168]. Ultimately, in a graphene monolayer, the energy gain due to the formation of new bonds is not sufficient to compensate for the large associated strain in the structure [176, 177][11]. Thus, this self-healing process is intimately linked to the larger flexibility found in nanostructures.

The time evolution of the electronic states during the ionic motion is presented in figure 15(b) as a series of contour maps depicting the norm of the excited electron wavefunction. As time progresses, we find the excited electron distribution to change from an anti-bonding to a dangling bond characteristic. We should emphasize that in contrast to conventional *ab initio* MD simulations, we monitor the time evolution of each populated and empty single-electron state during the ionic motion. This approach provides information not only about the charge distribution, but also the lifetime of electronic excitations in presence of ionic motion. An important indication for the onset of a non-adiabatic decay is a sudden increase in the off-diagonal matrix elements of the Kohn–Sham Hamiltonian in the basis of the time evolving eigenstates. Following such a non-adiabatic decay, rapid Rabi oscillations are known to appear in the electronic levels, even if the atomic motion is smooth [178].

With the charge distribution determined by the time-evolving populated states, forces acting on atoms are determined using the Hellmann–Feynman theorem [171, 172]. This approach offers a significant advantage over the conventional *ab initio* MD simulations, where forces acting on atoms are calculated from static solutions of the Kohn–Sham equations at each time step, presuming the population of each Kohn–Sham state is known. Predicting the correct sequence of populated levels is a challenging undertaking, especially in case of level alternation, which occurs in the single-electron spectrum following the electronic excitation, as shown in figure 16. In our system, we found the character of the hole wavefunction to differ significantly from the valence band character. Similarly, the character of the excited electron was found to differ from the conduction band states. Thus, the level alternation seen

---

[11] This agrees with a recent finding that apparently the only favourable reconstruction in defective graphite occurs by forming bonds in-between adjacent layers.
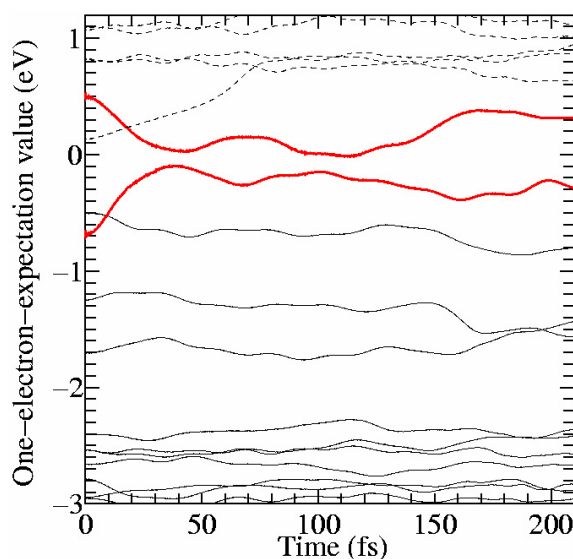
Figure 16. Time evolution of the energy spectrum during the atomic motion following the initial electronic excitation. Fully occupied states are denoted by solid black curves, completely empty states by dashed black curves. Time evolution of the electron–hole pair, created by the electronic excitation, is shown by the heavier solid curves. From [16], © Elsevier Publishers.

in figure 16 did not cause a non-adiabatic decay of the excitation, and the system remained on the adiabatic potential energy surface during our simulation.

Unlike in bulk systems, where electron–hole excitations typically decay on a femtosecond timescale, we did not find any indication for such a non-adiabatic decay of the excitation in the defective nanotube during our MD simulation, extending over 200 fs. We find the long lifetime of this excitation intimately linked to new electronic states associated with the vacancy, which do not couple to the valence and conduction bands of the nanotube. Due to the apparent long lifetime of the electronic excitation, a significant fraction of the ion dynamics occurs on the excited state potential energy surface, which differs significantly from the ground state potential energy surface. In defect-free nanotubes, electronic excitations decay much faster, and play only a negligible role in the atomic motion.

An important difference between ground and excited state dynamics concerns the activation barrier, which is absent in the electronically excited state, but has a value of 0.3 eV in the electronic ground state. Consequently, self-healing induced by electronic excitations should occur very quickly even at low temperatures. We find it intriguing that even excitations, which initially tend to destroy the structure at the defect site, may induce self-healing. Our most significant finding is that electronic excitations can be tuned to selectively repair defects, while leaving the remaining perfect structure intact, without inducing new defects.

As an alternative to the rapid excited state dynamics, several activated processes could occur in the electronic ground state. In view of the moderate activation barrier of 0.3 eV, a bond bridging the vacancy in a defective (3, 3) nanotube may form on the timescale of seconds at ambient temperature. This process occurs even faster at higher temperatures [179], since high-temperature dynamics often mimics on a short timescale the long-time behaviour at lower temperatures. At temperatures approaching the melting point, we may expect the nanotube to be destroyed, starting with a pre-melting near the vacancy site.

To obtain a rough insight into processes occurring at high temperatures, we performed Nosé–Hoover molecular dynamics simulations of a nanotube subject to a rapid temperature increase. Our preliminary findings [175] suggest that the defective nanotube remained intact even at temperatures comparable to the melting point of graphite [130]. At these very high temperatures, we observed the formation of bonds bridging the gap created by the monatomic vacancy, similar to those formed during the electronically induced self-healing. Since the system gained energy during this process, the reconstruction persisted after the structure had been cooled down.

5.2. Deoxidation of defective nanotubes

Oxidation is commonly used to purify carbon nanotubes (CNTs) from amorphous carbon soot (see, e.g., [180]). The efficiency of this process relies on the fact that carbon soot converts easily to CO and CO_2, which subsequently evaporate, in contrast to structurally perfect nanotubes and graphite, which are rather unreactive. *Ab initio* density functional theory (DFT) calculations [181, 182] indeed suggest that the interaction of molecular oxygen with carbon nanotubes should be weak, in stark contrast to the dissociative adsorption of oxygen atoms at the edges [183] and at defect sites [184] of carbon nanotubes. There, chemisorbed oxygen forms chemically strong C–O–C complexes, which have been observed by near-edge x-ray absorption fine-structure spectroscopy [185]. Whereas physisorption of O_2 causes hole doping and increases the electronic conductivity of semiconductor nanotubes [181], formation of C–O–C complexes destroys the perfect π-bonding network and thus decreases the conductivity of nanotubes. Finding an effective way to remove the chemisorbed oxygen is a necessary prerequisite for a practical use of carbon nanotubes in electronic devices.

Removal of the chemisorbed oxygen atoms by heat treatment comes with the inevitable side effect of damaging the carbon network surrounding the O atom, due to the higher stability of the C–O bond in comparison to C–C bonds [183]. Such structural damage is evidenced in temperature programmed mass spectra of oxidized carbon nanohorns [186], with a graphitic network similar to nanotubes, which show a preferential desorption of CO and CO_2 molecules rather than oxygen at high temperatures. The stability of the C–O bond also makes alternative chemical processes, designed to selectively breaking the C–O bond, very unlikely. The inertness of the C–O–C complex in a defective nanotube was confirmed by our DFT calculations, which suggest that H atoms preferentially attach to carbon rather than oxygen sites. Similar to the observed disintegration of H_2O molecules by a resonant Auger process [187], a photo-chemical deoxidation of nanotubes is reported here as a viable alternative to chemical and thermal purification methods [17].

Results of first-principles simulations for electron ion dynamics (FPSEID) [171, 172] suggest that the strong C–O bonds can be efficiently ruptured by optically promoting the bonding electrons into an excited state by a resonant Auger process. Similar to results of photo-induced reconstruction at vacancy sites in nanotubes, reported above, we find photoexcitations in these defective nanostructures to last sufficiently long to cause breaking and formation of covalent bonds. In the case of oxygen covalently bonded to defect sites, selective photoexcitation may initiate the desorption of the oxygen atom with no damage to the surrounding carbon network.

Our study of the photodesorption process is based on *ab initio* molecular dynamics (MD) simulations on the adiabatic potential energy surface (APES) associated with an electronically excited state. To correctly follow the APES we have combined time-dependent DFT (TDDFT) [11] with classical Newton equations of motion for the ions in FPSEID [171, 172], similar to the OCTOPUS approach [188]. This type of computational approach turns out
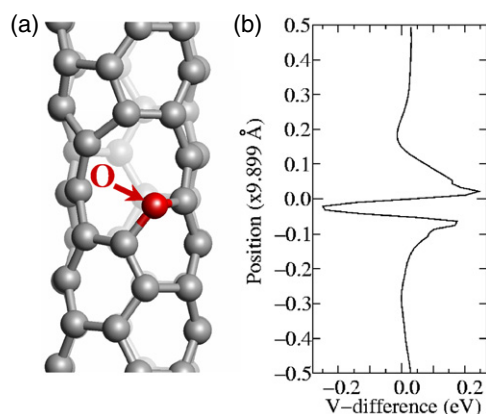
Figure 17. (a) Structure of the C–O–C complex in a defective C(3, 3) nanotube. (b) Difference between the self-consistent LDA potential V of the structure in (a), containing the C–O–C complex, and a reference structure with no oxygen, but all carbons in the same positions. V—*difference* is averaged in the plane normal to the tube axis and does not contain contributions from the non-local part of the pseudopotentials. The same vertical length scale is used in (a) and (b). From [17], © American Physical Society.

to be particularly challenging, since the study precludes the solution of the time-dependent Schrödinger equation for the time evolution of the electronic wavefunctions in the presence of ionic motion, caused by the changing charge distribution. This scheme is valid unless the system significantly deviates from the APES due to a non-radiative decay of the excited state. The main benefit of the TDDFT approach is its ability to correctly populate the electronic states even in case of level alternation. We applied the local density approximation [70, 71] to DFT, and confirmed the validity of our photodesorption results by using the alternative GGA form [189][12] for the exchange–correlation functional. We described the interaction between valence electrons and ions by separable norm-conserving pseudopotentials [72, 73], and used a plane wave basis with a cutoff energy of 60 Ryd in all the calculations.

As in the previously discussed case of monovacancies, we have focused on the C(3, 3) armchair nanotube, one of the thinnest nanotubes synthesized to date [173, 174, 190]. We have imposed three dimensional periodic boundary conditions, effectively describing a nanotube bundle with triangular packing and an inter-wall distance of 4 Å. To minimize coupling between defect sites, we used four primitive unit cells of the pristine (3, 3) nanotube as a unit cell in the axial direction, as shown in figure 17(a), and used the Γ point to sample the one-dimensional Brillouin zone.

The starting point of all APES simulations of the photo-excitation process, described in the following, was the equilibrated structure of the oxidized nanotube in the electronic ground state depicted in figure 17(a). The formation of a pentagon opposite the oxygen adsorption site was found energetically favourable due to the saturation of dangling bonds. The effect of the oxygen atom on the self-consistent potential of the defective tube is demonstrated in figure 17(b). The presence of the O atom causes a sharp dip in the potential, which leads to a strong scattering and trapping of carriers near the C–O–C complex, thus decreasing the nanotube conductance as mentioned before.

---

[12] We have found that our results do not depend strongly on the exchange–correlation functional used in DFT. The forces acting on the oxygen atom in the Auger final state, obtained using the GGA, were generally stronger than LDA-based forces. Consequently, the predicted photo-induced oxygen desorption is activation-free both in the GGA and LDA, and should occur even faster in a GGA than in our LDA simulation.
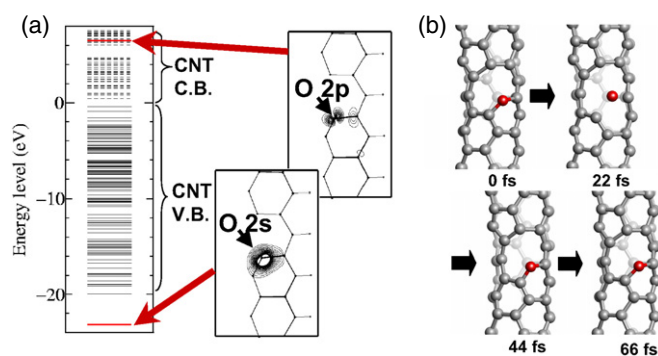
Figure 18. (a) Electronic structure of the system in figure 17(a). Valence states at the Γ point are shown by solid lines, conduction states by dashed lines. The insets show the charge density maps corresponding to the O 2s level, lying below the nanotube valence band, and the O 2p level, lying within the nanotube conduction band. (b) Time evolution of the C–O–C complex following an O 2s → O 2p excitation. From [17], © American Physical Society.

In order to investigate the possibility of photodesorbing the oxygen atom, we considered a sudden electronic excitation from the localized O 2s orbital in the frozen ground state geometry. The electronic spectrum of this system is shown in figure 18(a). We find the O 2s level to lie well below the nanotube valence band. The O 2p state, on the other hand, hybridizes strongly with C 2p states, forming a bonding and an antibonding state. Close inspection of the oxygen-related states, represented in the insets in figure 18(a), suggests that the O 2s state has a bonding character and hybridizes only moderately with the 2p orbitals of the neighbouring C atoms. The O 2p–C 2p hybrid state, which lies in resonance with the nanotube conduction band, shows an antibonding character[13]. Consequently, we would expect the O 2s → O 2p excitation, requiring a vertical excitation energy of 33 eV,[14] to weaken the C–O bond and to cause a possible desorption of the oxygen atom.

The structure evolution during this photo-excitation process, as obtained by the FPSEID simulation, is shown by several snapshots in figure 18(b). Our results indicate that following the O 2s → O 2p photo-excitation, the C–O bond length extends significantly from 1.40 to 1.90 Å. In spite of this large bond elongation, the C–O–C complex remains intact without any indication of O-emission. We expect that such excitations should only heat up the nanotube, but should not trigger a desorption of the chemisorbed oxygen.

As a viable alternative to this photo-excitation, we studied the resonant Auger process, initiated by exciting one O1s core electron to the O 2p level, requiring an energy of ≈530 eV [185]. The subsequent Auger process of interest in the present context, depicted in figure 19(a),[15] leads to a final state with two holes in the O 2s level[16]. As we will show in the following, this final state electronic configuration will cause a spontaneous emission of the O atom and a subsequent self-healing of the created vacancy due to the formation of a new C–C bond.

---

[13] This character analysis is based on calculated overlaps with the wavefunctions of an oxygen pseudo-atom [72, 73].

[14] The calculated excitation energy of 33 eV is based on the total energy difference between the ground and the excited state within LDA.

[15] In our simplified description, we exclude the four valence electrons in the O 2p level from the discussion, since they are not affected by the Auger process.

[16] To treat adequately the +1e net charge per unit cell in the Auger final state, we superposed a uniform negative background charge to keep the system charge neutral. The negative background charge was treated separately from the real charges in the system to avoid fictitious Coulomb interactions, which may otherwise cause artifacts in systems with periodic boundary conditions.
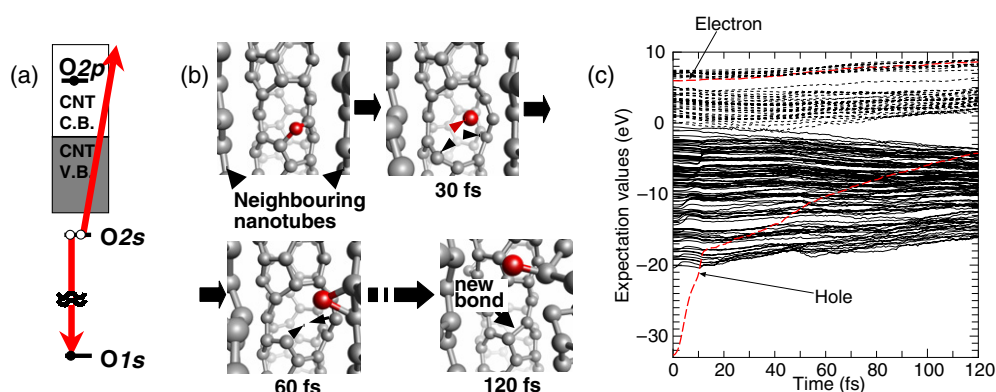
Figure 19. (a) Schematics of the resonant Auger decay following an initial O 1s → O 2p excitation, with two holes in the O 2s and one extra electron in the O 2p level in the final state (see footnote 14). The arrows depict the relaxation of the O1s hole, followed by the emission of the O 2s electron. Also shown is the position of the relevant oxygen levels with respect to the valence band (VB) and the conduction band (CB) of the nanotube. (b) Snapshots of the MD simulation starting from the Auger state shown in (a). Arrows are used to guide the eye when following the atomic motion. (c) Time evolution of the expectation value of all single particle states throughout the entire MD simulation. The heavy dashed curves denote the evolution of the initially excited electron (upper curve) and the two holes (lower curve). Conduction band states of the nanotube are shown by the dotted lines. From [17], © American Physical Society.

We assume that the Auger process spontaneously follows the O1s → O 2p photo-excitation and starts the simulation in the Auger state shown in figure 19(a) (see footnote 14). Figure 19(b) shows snapshots of the MD simulation of the oxidized C(3, 3) nanotube, depicting the O-emission from the C–O–C complex. Only 30 fs after the photo-excitation, we observe the initial escape of the O atom from the nanotube. Meanwhile, the two C neighbours are pushed back, initially enlarging the vacancy size. Another 30 fs later, these C atoms change their direction of motion and start approaching each other. 120 fs after the photo-excitation, the two carbon atoms approach sufficiently to form a new bond, indicative of a self-healing mechanism, which had been postulated to occur in thin carbon nanotubes [16, 175].

The time evolution of the expectation values of all single particle states throughout the MD simulation is shown in figure 19(c). Upon depopulation at $t = 0$, the energy eigenvalue of the O 2s level drops by more than 10 eV with respect to its value in the ground state shown in figure 18(a)[17]. This drop is followed by its rapid rise into the nanotube valence band region during the first 10 fs. The observed alternation of the O 2s level with nanotube bands is generally expected to cause a non-adiabatic decay of the excitation. This decay does not occur in our simulation due to the weak overlap between the O 2s orbital and the nanotube valence states. Consequently, the excited state dynamics follows the corresponding adiabatic potential energy surface for an extended time period.

The main benefit of the state with a completely depopulated O 2s level is its long lifetime, which we found to be crucial for the O emission. The long lifetime, depicted in figure 19(c), is caused by the spatial separation between the O 2s orbital and the nanotube valence wavefunctions. Similar long lifetimes of the order of 10^{-13} s of O 2s holes were

---

[17] The substantial drop in the O 2s orbital energy following its depopulation in the O-CNT system can be compared to the behaviour of an isolated atom. There, both LDA and GGA suggest a similar O 2s orbital lowering, after a neutral oxygen atom with the electronic configuration O $1s^2 2s^2 2p^4$ has acquired a single positive charge in the O $1s^2 2s^0 2p^5$ state.
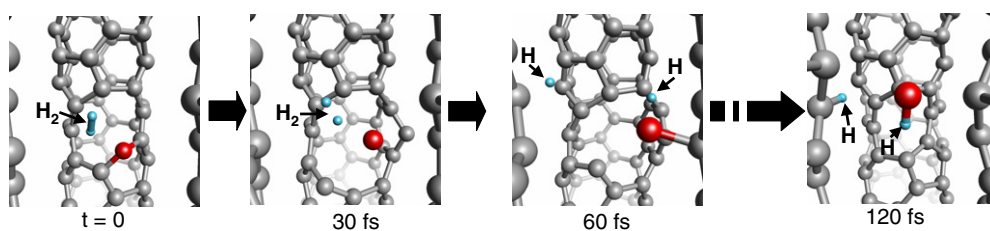
Figure 20. Dynamics of the C–O–C complex in the presence of a H$_2$ molecule, starting from the same Auger final state as considered in figure 19. From [17], © American Physical Society.

also reported during the reactions of ionized O atoms with Pt(111) [191] and TiC(111) [192] surfaces, and should also remain a common feature in other carbon nanotubes.

As shown in figure 19(b), the ejection of the O atom from the C–O–C complex occurs without any adverse effect on the carbon network. When occurring in a bundle, represented by the boundary conditions in our simulation, the ejected O atom may re-adsorb at a neighbouring tube. This process indeed occurs 120 fs after the photo-excitation, as seen in figure 19(b). To help prevent the oxygen from re-adsorbing on a nanotube, we consider ways to render oxygen less reactive. A viable scenario would be exposing the oxidized nanotube to an H$_2$ atmosphere, with the hope forming H$_2$O molecules following the deoxidation process.

The results of our corresponding simulation with one H$_2$ molecule per unit cell are shown as a series of snapshots in figure 20. We find that the spontaneous photo-desorption of the oxygen atom in the Auger state shown in figure 19(a) (see footnote 14) proceeds in a similar way to the process depicted in figure 19(b). Rather than re-adsorbing on a nanotube, the O atom reacts with H$_2$ and forms an OH$^+$ radical. We expected this OH$^+$ radical to eventually neutralize and react with the lone H atom to form a water molecule, but we did not observe this reaction in the limited time period of our simulation. In spite of the uncertainty about the final state of the desorbed oxygen, our results strongly indicate that exposing the oxidized nanotube to an H$_2$ atmosphere during the resonant Auger process is an efficient way to deoxidize nanotubes and prevent their re-oxidation (see footnote 12).

6. Summary and conclusions

The examples quoted in this contribution illustrate some of the intriguing problems associated with carbon nanostructures, and current computational approaches used to address them. The foremost intention was to demonstrate the capability of current numerical techniques to provide quantitative understanding of physical processes in nanostructures. Such calculations ideally complement experimental observations, which are subject to fundamental limitations in the quantum regime. The complexity of the observed phenomena, on the other hand, makes experimental observations indispensable in the search for the origin of phenomena associated with carbon nanostructures.

These unexpected phenomena included the exceptionally high thermal conductance of nanotubes, a consequence of their quasi-1D structure, hard optical phonon frequencies, and large phonon mean free path. Trivalent carbon radicals may be sterically stabilized in specific sp^2 bonded carbon nanostructures, resulting in a net magnetization. Carbon nanotubes exhibit thermal contraction even well beyond room temperature, and may even be used as a nanoscale counterpart of a velcro bond. Nanotube peapods, formed by encapsulation of fullerenes or other molecules in nanotubes, emerge as intriguing nanostructures with many potential applications,

including a computer memory or nanoscale chemical reactors. Fullerenes, nanotubes, and other sp^2 bonded carbon nanostructures may undergo large-scale morphological changes, including fusion, as a result of sequential Stone–Wales bond rotations. Defective nanotubes exhibit an unexpected self-healing ability at elevated temperatures and in the electronically excited state. Due to their unusually long lifetime, electronic excitations may be used to selectively remove oxygen impurities from nanotubes.

Acknowledgments

References

[1] Feynman R P 1959 *Annual Mtg of the American Physical Society (California Institute of Technology, Dec. 1959)* reprinted in '*The Pleasure of Finding Things Out*' ed J Robbins (New York: Perseus Books, 1999)
[2] Oberlin A, Endo M and Koyama T 1976 *J. Cryst. Growth* **32** 335
[3] Kroto H W, Heath J R, O'Brien S C, Curl R F and Smalley R E 1985 *Nature* **318** 162
[4] Iijima S 1991 *Nature* **354** 56
[5] Tománek D, Zhong W and Krastev E 1993 *Phys. Rev.* B **48** 15461
[6] Hohenberg P and Kohn W 1964 *Phys. Rev.* B **136** 864
[7] Kohn W and Sham L 1965 *Phys. Rev.* A **140** 1133
[8] Perdew J P, Chevary J, Vosko S, Jackson K A, Pederson M R, Singh D J and Fiolhais C 1992 *Phys. Rev.* B **46** 6671–87
[9] Stott M and Zaremba E 1980 *Phys. Rev.* A **21** 12–23
[10] Zangwill A and Soven P 1980 *Phys. Rev.* A **21** 1561–72
[11] Runge E and Gross E K U 1984 *Phys. Rev. Lett.* **52** 997
[12] Tománek D and Schluter M A 1991 *Phys. Rev. Lett.* **67** 2331
[13] Zhong W, Tománek D and Bertsch G 1993 *Solid State Commun.* **86** 607
[14] Tersoff J 1988 *Phys. Rev. Lett.* **61** 2879

[15] Tersoff J 1988 *Phys. Rev.* B **37** 6991
[16] Miyamoto Y, Berber S, Yoon M, Rubio A and Tománek D 2004 *Chem. Phys. Lett.* **392** 209
[17] Miyamoto Y, Jinbo N, Nakamura H, Rubio A and Tománek D 2004 *Phys. Rev.* B **70** 233408
[18] Wei L, Kuo P, Thomas R, Anthony T and Banholzer W 1993 *Phys. Rev. Lett.* **70** 3764
[19] Dresselhaus M, Dresselhaus G and Eklund P 1996 *Science of Fullerenes and Carbon Nanotubes* (San Diego, CA: Academic)
[20] Berber S, Kwon Y-K and Tománek D 2000 *Phys. Rev. Lett.* **84** 4613
[21] Uher C 1991 *Landolt–Börnstein: Numerical Data and Functional Relationships in Science and Technology* (*New Series* Group III, vol 15c) ed O Madelung and G K White (Berlin: Springer) pp 426–48
[22] Hone J, Whitney M, Piskoti C and Zettl A 1999 *Phys. Rev.* B **59** R2514
[23] Hone J, Whitney M and Zettl A 1999 *Synth. Met.* **103** 2498
[24] McQuarrie D 1976 *Statistical Mechanics* (London: Harper and Row)
[25] Schoen M and Hoheisel C 1985 *Mol. Phys.* **56** 653
[26] Levesque D and Verlet L 1987 *Mol. Phys.* **61** 143
[27] Maeda A and Munakata T 1995 *Phys. Rev.* E **52** 234
[28] Evans D 1982 *Phys. Lett.* A **91** 457
[29] Hansen D and Evans D 1994 *Mol. Phys.* **81** 767
[30] Rapaport D 1998 *The Art of Molecular Dynamics Simulation* (Cambridge: Cambridge University Press)
[31] Nosé S 1984 *Mol. Phys.* **52** 255
[32] Anthony T, Banholzer W, Fleischer J F, Wei L, Kuo P, Thomas R and Pryor R 1990 *Phys. Rev.* B **42** 1104
[33] Nihira T and Iwata T 1975 *Japan. J. Appl. Phys.* **14** 1099
[34] Holland M, Klein C and Straub W 1966 *J. Phys. Chem. Solids* **27** 903
[35] de Combarieu A 1967 *J. Physique* **28** 951
[36] Kwon Y-K, Berber S and Tománek D 2004 *Phys. Rev. Lett.* **92** 015901
[37] Kubo R 1946 *Rubber Elasticity* (Tokyo: Kawade Shobo Shinsha)
[38] White G and Choy C 1984 *J. Polym. Sci. Polym. Phys. Edn.* **22** 835
[39] Riley D 1945 *Proc. Phys. Soc. London* **57** 486
[40] Morgan W 1972 *Carbon* **10** 73
[41] Belenkii G, Salaev E, Suleimanov R, Abdullaev N and Shteinshraiber V 1985 *Solid State Commun.* **53** 967
[42] Roy R and Agrawal D 1997 *Nature* **388** 433
[43] Mary T, Evans J, Vogt T and Sleight A 1996 *Science* **272** 90
[44] Hoover W 1985 *Phys. Rev.* A **31** 1695
[45] Raravikar N, Keblinski P, Rao A, Dresselhaus M, Schadler L and Ajayan P 2002 *Phys. Rev.* B **66** 235424
[46] Schelling P K and Keblinski P 2003 *Phys. Rev.* B **68** 035425
[47] Thess A *et al* 1996 *Science* **273** 483
[48] Baughman R H and Soldatov A 1999 private communication
[49] Reynolds W N 1968 *Physical Properties of Graphite* (Amsterdam: Elsevier)
[50] Ashcroft N and Mermin N 1976 *Solid State Physics* (New York: Holt, Rinehart and Winston)
[51] Lang L, Doyen-Lang S, Charlier A and Charlier M 1994 *Phys. Rev.* B **49** 5672
[52] Hone J, Batlogg B, Benes Z, Johnson A and Fischer J 2000 *Science* **289** 1730
[53] Kwon Y-K and Tománek D 2000 *Phys. Rev. Lett.* **84** 1483
[54] Mintmire J, Dunlap B and White C 1992 *Phys. Rev. Lett.* **68** 631
[55] Saito R, Fujita M, Dresselhaus G and Dresselhaus M 1992 *Appl. Phys. Lett.* **60** 2204
[56] Hamada N, Sawada S and Oshiyama A 1992 *Phys. Rev. Lett.* **68** 1579
[57] Schluter M, Lannoo M, Needels M, Baraff G and Tománek D 1992 *Phys. Rev. Lett.* **68** 526
[58] Makarova T L, Sundqvist B, Höhne R, Esquinazi P, Kopelevich Y, Scharff P, Davydov V A, Kashevarova L S and Rakhmanina A V 2001 *Nature* **413** 716
[59] Park N, Yoon M, Berber S, Ihm J, Osawa E and Tománek D 2003 *Phys. Rev. Lett.* **91** 237204
[60] Rode A V, Gamaly E G, Christy A G, Gerald J G F, Hyde S T, Elliman R G, Luther-Davies B, Veinger A I, Androulakis J and Giapintzakis J 2004 *Phys. Rev.* B **70** 054407
[61] Mackay A L and Terrones H 1991 *Nature* **352** 762
[62] Vanderbilt D and Tersoff J 1992 *Phys. Rev. Lett.* **68** 511
[63] Bursill L A and Bourgeois L 1995 *Phys. Lett.* B **9** 1461
[64] Hyde S T and O'Keeffe M 1996 *Phil. Trans. R. Soc.* A **354** 1999
[65] Rode A V, Hyde S T, Gamaly E G, Elliman R G, McKenzie D R and Bulcock S 1999 *Appl. Phys.* A **69** S755
[66] Rode A V, Gamaly E G and Luther-Davies B 2000 *Appl. Phys.* A **70** 135
[67] Fujita M, Wakabayashi K, Nakada K and Kusakabe K 1996 *J. Phys. Soc. Japan* **65** 1920
[68] Nakada K, Fujita M, Dresselhaus G and Dresselhaus M S 1996 *Phys. Rev.* B **54** 17954

[69] Kusakabe K and Maruyama M 2003 *Phys. Rev.* B **67** 092406
[70] Ceperley D M and Alder B J 1980 *Phys. Rev. Lett.* **45** 566
[71] Perdew J P and Zunger A 1981 *Phys. Rev.* B **23** 5048
[72] Troullier N and Martins J L 1991 *Phys. Rev.* B **43** 1993
[73] Kleinman L and Bylander D M 1982 *Phys. Rev. Lett.* **48** 1425
[74] Sankey O F and Niklewski D J 1989 *Phys. Rev.* B **40** 3979
[75] Park N, Lee K, Han S, Yu J and Ihm J 2002 *Phys. Rev.* B **65** 121405
[76] Scheffler M, Vigneron J P and Bachelet G B 1985 *Phys. Rev.* B **31** 6541
[77] Balaban A T, Klein D J and Folden C A 1994 *Chem. Phys. Lett.* **217** 266
[78] Gomberg M 1900 *J. Am. Chem. Soc.* **22** 757
[79] Haddon R C 1975 *Nature* **256** 394
[80] Itkis M E, Chi X, Cordes A W and Haddon R C 2002 *Science* **296** 1443
[81] Overney G, Zhong W and Tománek D 1993 *Z. Phys.* D **27** 93
[82] Treacy M, Ebbesen T and Gibson J 1996 *Nature* **381** 678
[83] Falvo M R, Clary G J, Taylor R M, Chi V, Brooks F P, Washburn S and Superfine R 1997 *Nature* **389** 582
[84] Yakobson B I, Brabec C and Bernholc J 1996 *Phys. Rev. Lett.* **76** 2511
[85] Lu J P 1997 *Phys. Rev. Lett.* **79** 1297
[86] Iijima S and Ichihashi T 1993 *Nature* **363** 603
[87] Bethune D, Kiang C, de Vries M, Gorman G, Savoy R, Vazquez J and Beyers R 1993 *Nature* **363** 605
[88] Saito R, Dresselhaus G and Dresselhaus M S 1996 *Phys. Rev.* B **53** 2044
[89] Iijima S 1994 *Mater. Res. Soc. Bull.* **19** 43
[90] Gabriel J-C 2003 private communication
[91] Dunlap B 1992 *Phys. Rev.* B **46** 1933
[92] Charlier J C, Ebbesen T W and Lambin P 1996 *Phys. Rev.* B **53** 11108
[93] Berber S, Kwon Y-K and Tománek D 2003 *Phys. Rev. Lett.* **91** 165503
[94] Tománek D, Enbody R J and Kwon Y-K 1998 Micro-fastening system and method of manufacture *US Patent Application* (filed February 12, 1998)
[95] Fahy S, Louie S and Cohen M 1986 *Phys. Rev.* B **34** 1191
[96] Simonis P, Volodin A, Seynaeve E, Lambin P and Haesendonck C V 2000 *Science and Application of Nanotubes* ed D Tománek and R J Enbody (New York: Kluwer–Academic) p 83
[97] Hayashida T, Pand L and Nakayama Y 2002 *Physica* B **323** 352
[98] Chen X, Zhang S, Dikin D A, Ding W, Ruoff R S, Pan L and Nakayama Y 2003 *Nano Lett.* **3** 1299
[99] Smith B, Monthioux M and Luzzi D 1998 *Nature* **396** 323
[100] Burteaux B, Claye A, Smith B, Monthioux M, Luzzi D and Fischer J 1999 *Chem. Phys. Lett.* **310** 21
[101] Smith B, Monthioux M and Luzzi D 1999 *Chem. Phys. Lett.* **315** 31
[102] Smith B W and Luzzi D E 2000 *Chem. Phys. Lett.* **321** 169
[103] Hirahara K, Suenaga K, Bandow S, Kato H, Okazaki T, Shinohara H and Iijima S 2000 *Phys. Rev. Lett.* **85** 5384
[104] Kwon Y-K, Tománek D and Iijima S 1999 *Phys. Rev. Lett.* **82** 1470
[105] Service R F 2001 *Science* **292** 45
[106] McIntosh G C, Yoon M, Berber S and Tománek D 2004 *Phys. Rev.* B **70** 045401
[107] McIntosh G C, Tománek D and Park Y W 2003 *Phys. Rev.* B **67** 125419
[108] Han S, Yoon M, Berber S, Park N, Osawa E, Ihm J and Tománek D 2004 *Phys. Rev.* B **70** 113402
[109] Girifalco L A, Hodak M and Lee R S 2000 *Phys. Rev.* B **62** 13104
[110] Hodak M and Girifalco L A 2001 *Phys. Rev.* B **64** 35407
[111] Berber S, Kwon Y-K and Tománek D 2002 *Phys. Rev. Lett.* **88** 185502
[112] Monthioux M, Smith B W, Burteaux B, Claye A, Fischer J E and Luzzi D E 2001 *Carbon* **39** 1251
[113] Okada S, Saito S and Oshiyama A 2001 *Phys. Rev. Lett.* **86** 3835
[114] Bandow S, Takizawa M, Hirahara K, Yudasaka M and Iijima S 2001 *Chem. Phys. Lett.* **337** 48
[115] Yakobson B and Smalley R 1997 *Am. Sci.* **85** 324
[116] Li Y and Tománek D 1994 *Chem. Phys. Lett.* **221** 453
[117] Lou L, Nordlander P and Smalley R E 1995 *Phys. Rev.* B **52** 1429
[118] Kim S, Lee Y, Nordlander P and Tománek D 1997 *Chem. Phys. Lett.* **264** 345
[119] Lee Y, Kim S and Tománek D 1997 *Chem. Phys. Lett.* **265** 667
[120] Kwon Y-K, Tománek D, Lee Y H, Lee K H and Saito S 1998 *J. Mater. Res.* **13** 2363
[121] Kim S and Tománek D 1994 *Phys. Rev. Lett.* **72** 2418
[122] Kwon Y-K, Lee Y H, Kim S G, Jund P, Tománek D and Smalley R E 1997 *Phys. Rev. Lett.* **79** 2065
[123] Busmann H-G, Lill T and Hertel I 1991 *Chem. Phys. Lett.* **187** 459

[124] Meletov K P, Assimopoulos S, Tsilija I, Kourouklis G A, Arvanitidis J, Ves S, Sundqvist B and Wagberg T 2001 *Chem. Phys. Lett.* **341** 435

[125] Meletov K P, Arvanitidis J, Assimopoulos S, Kourouklis G A and Sundqvist B 2002 *J. Exp. Theor. Phys.* **95** 736

[126] Blank V D, Buga S G, Serebryanaya N R, Denisov V N, Dubitsky G A, Ivlev A N, Mavrin B N and Popov M Y 1995 *Phys. Lett.* A **205** 208

[127] Serebryanaya N R and Chernozatonskii L A 2000 *Solid State Commun.* **114** 537

[128] Serebryanaya N R, Blank V D, Ivdenko V A and Chernozatonskii L A 2001 *Solid State Commun.* **118** 183

[129] Talyzin A V, Dubrovinsky L S, Oden M, Bihan T L and Jansson U 2002 *Phys. Rev.* B **66** 165409

[130] Ronchi C, Beukers R, Heinz H, Hiernaut J P and Selfslag R 1992 *Int. J. Thermophys.* **13** 107

[131] Terrones M, Terrones H, Banhart F, Charlier J-C and Ajayan P M 2000 *Science* **288** 1226

[132] Kim Y-H, Choi J, Chang K J and Tománek D 2003 *Phys. Rev.* B **68** 125420

[133] Osawa E, Ueno H, Yoshida M, Slanina Z, Zhao X, Nishiyama M and Saito H 1998 *J. Chem. Soc. Perkin Trans.* **2** 943

[134] Kim Y-H, Lee I-H, Chang K J and Lee S 2003 *Phys. Rev. Lett.* **90** 65501

[135] Stone A J and Wales D J 1986 *Chem. Phys. Lett.* **128** 501

[136] Kumeda Y and Wales D J 2003 *Chem. Phys. Lett.* **374** 125

[137] Zhao Y F, Yakobson B I and Smalley R E 2002 *Phys. Rev. Lett.* **88** 185501

[138] Zhao Y F, Smalley R E and Yakobson B I 2002 *Phys. Rev.* B **66** 195409

[139] Ueno H, Osawa S, Osawa E and Takeuchi K 1998 *Fullerene Sci. Technol.* **6** 319

[140] Rao A M *et al* 1997 *Appl. Phys.* A—*Mat. Sci. Proc.* **64** 231

[141] Honda K, Osawa E, Slanina Z and Matsumoto T 1996 *Fullerene Sci. Technol.* **4** 819

[142] Osawa S, Sakai M and Osawa E 1997 *J. Phys. Chem.* A **101** 1378

[143] Strout D, Murry R, Xu C, Eckhoff W, Odom G and Scuseria G 1993 *Chem. Phys. Lett.* **241** 576

[144] E W, Ren W and Vanden-Eijnden E 2002 *Phys. Rev.* B **66** 052301

[145] Yoon M *et al* 2004 *Phys. Rev. Lett.* **92** 075504

[146] Kaxiras E and Pandey K C 1988 *Phys. Rev. Lett.* **61** 2693

[147] Eggen B R, Heggie M I, Jungnickel G, Latham C D, Jones R and Briddon P R 1996 *Science* **272** 87

[148] Slanina Z, Zhao X, Uhlik F, Ozawa M and Osawa E 2000 *J. Organometal. Chem.* **599** 57

[149] Banhart F 1999 *Rep. Prog. Phys.* **62** 1181

[150] Bettinger H, Yakobson B and Scuseria G 2003 *J. Am. Chem. Soc.* **125** 5572

[151] Murry R L, Strout D L, Odom G K and Scuseria G E 1993 *Nature* **366** 665

[152] Scuseria G E 1996 *Science* **271** 942

[153] Osawa E, Slanina Z, Honda K and Zhao X 1998 *Fullerene Sci. Technol.* **6** 259

[154] Heiney P A, Fischer J E, McGhie A R, Romanow W J, Denenstein A M, McCauley J P, Smith A B and Cox D E 1991 *Phys. Rev. Lett.* **66** 2911

[155] Okazaki T, Okazaki T, Suenaga K, Hirahara K, Bandow S, Iijima S and Shinohara H 2001 *J. Am. Chem. Soc.* **123** 9673

[156] Wang Y, Tománek D and Bertsch G F 1991 *Phys. Rev.* B **44** R6562

[157] Osawa E and Honda K 1996 *Fullerene Sci. Technol.* **4** 939

[158] Fowler P W and Manolopoulos D E 1995 *An Atlas of Fullerenes* (Oxford: Clarendon)

[159] Press W, Teukolsky T, Vetterling W T and Flannery B P 1986 *Numerical Recipes* (Cambridge: Cambridge University Press)

[160] Nardelli M B, Yakobson B I and Bernholc J 1998 *Phys. Rev. Lett.* **81** 4656–9

[161] Nardelli M B, Yakobson B and Bernholc J 1998 *Phys. Rev.* B **57** R4277–80

[162] Zhang P, Lammert P E and Crespi V 1998 *Phys. Rev. Lett.* **81** 5346–9

[163] Ball P 1994 *Designing the Molecular World* (Princeton, NJ: Princeton University Press)

[164] Collins P C, Arnold M S and Avouris P 2001 *Science* **292** 706

[165] Appenzeller J, Martel R, Derycke V, Radosavjevic M, Wind S, Neumayer D and Avouris P 2002 *Microelectron. Eng.* **64** 391

[166] Martel R, Derycke V, Lavoie C, Appenzeller J, Chan K K, Tersoff J and Avouris P 2001 *Phys. Rev. Lett.* **87** 256805

[167] Igami M, Nakanishi T and Ando T 1999 *J. Phys. Soc. Japan* **68** 716

[168] Choi H J, Ihm J, Louie S G and Cohen M L 2000 *Phys. Rev. Lett.* **84** 2917

[169] Blöchl P E and Stathis J H 1999 *Phys. Rev. Lett.* **83** 372

[170] Yokozawa A and Miyamoto Y 2000 *J. Appl. Phys.* **88** 4542

[171] Sugino O and Miyamoto Y 1999 *Phys. Rev.* B **59** 2579

[172] Sugino O and Miyamoto Y 2002 *Phys. Rev.* B **66** 89901 (erratum)

[173] Qin L C, Zhao X L, Hirahara K, Miyamoto Y, Ando Y and Iijima S 2000 *Nature* **408** 50
[174] Wang N, Tang Z K, Li G D and Chen J S 2000 *Nature* **408** 50
[175] Miyamoto Y, Berber S, Yoon M, Rubio A and Tománek D 2002 *Physica* B **323** 78
[176] Telling R H, Ewels C P, El-Barbary A A and Heggie M I 2003 *Nat. Mater.* **2** 333
[177] El-Barbary A A, Telling R H, Ewels C P, Heggie M I and Briddon P R 2003 *Phys. Rev.* B **68** 144107
[178] See, for example, Fig. 3 in Miyamoto Y 2001 *Solid State Commun.* **117** 727
[179] Ajayan P M, Ravikumar V and Charlier J-C 1998 *Phys. Rev. Lett.* **81** 1437
[180] Gajewski S, Maneck H, Knoll U, Neubert D, Dörfel I, Mach R, Strauß B and Friedrich J F 2003 *Diamond Relat. Mater.* **12** 816
[181] Jhi S H, Louie S G and Cohen M L 2000 *Phys. Rev. Lett.* **85** 1710
[182] Giannozzi P, Car R and Scoles G 2003 *J. Chem. Phys.* **118** 1003
[183] Zhu X Y, Lee S M, Lee Y H and Frauenheim T 2000 *Phys. Rev. Lett.* **85** 2757
[184] Mazzoni M S C, Chacham H, Ordejón P, Sánchez-Portal D, Soler J M and Artacho E 1999 *Phys. Rev.* B **60** 2208(R)
[185] Kuznetsova A, Popova I, Yates J J T, Bronikowski M J, Huffman C B, Liu J, Smalley R E, Hwu H H and Chen J G 2001 *J. Am. Chem. Soc.* **123** 10699
[186] Bekyarova E, Hanzawa Y, Kaneko K, Silverstre-Alberto J, Sepulvda-Escribano A, Rodirguez-Peinoso F, Kasuya D, Yudasaka M and Iijima S 2002 *Chem. Phys. Lett.* **366** 463
[187] Nagasono M, Mase K, Tanaka S and Uritsu T 1998 *Chem. Phys. Lett.* **298** 141
[188] Marques M A L, Castro A, Bertsch G F and Rubio A 2003 *Comput. Phys. Commun.* **151** 60
[189] Perdew J P and Wang Y 1992 *Phys. Rev.* B **45** 13244
[190] Hayashi T, Kim Y, Matoba T, Esaka M, Nishimura K, Tsukada T, Endo M and Dresselhaus M 2003 *Nano Lett.* **3** 887
[191] Souda R, Yamamoto K, Hayami W, Aizawa T and Ishizawa Y 1995 *Phys. Rev.* B **51** 4463
[192] Souda R, Kawanowa H, Otani S and Aizawa T 2000 *J. Chem. Phys.* **112** 979